UC-34D
LBL-20463 c.1

Lawrence Berkeley Laboratory

UNIVERSITY OF CALIFORNIA

RECEIVED
LAWRENCE
BERKELEY LABORATORY

DEC 13 1985

LIBRARY AND
DOCUMENTS SECTION

Physics Division

PROPERTIES OF HEAVY QUARK JETS PRODUCED BY
e^+e^- ANNIHILATION AT 29 GeV

P.C. Rowson
(Ph.D. Thesis)

October 1985

For Reference

Not to be taken from this room

LBL-20463 c.1

Prepared for the U.S. Department of Energy under Contract DE-AC03-76SF00098

DISCLAIMER

This document was prepared as an account of work sponsored by the United States Government. While this document is believed to contain correct information, neither the United States Government nor any agency thereof, nor the Regents of the University of California, nor any of their employees, makes any warranty, express or implied, or assumes any legal responsibility for the accuracy, completeness, or usefulness of any information, apparatus, product, or process disclosed, or represents that its use would not infringe privately owned rights. Reference herein to any specific commercial product, process, or service by its trade name, trademark, manufacturer, or otherwise, does not necessarily constitute or imply its endorsement, recommendation, or favoring by the United States Government or any agency thereof, or the Regents of the University of California. The views and opinions of authors expressed herein do not necessarily state or reflect those of the United States Government or any agency thereof or the Regents of the University of California.

LBL-20463

Properties of Heavy Quark Jets Produced by e^+e^- Annihilation at 29 GeV

Peter Cavanagh Rowson
(Ph.D. Thesis)

Lawrence Berkeley Laboratory
University of California
Berkeley, California 94720

October 1985

This work was supported by the Director, Office of Energy Research, Office of High Energy and Nuclear Physics, Division of High Energy Physics of the U.S. Department of Energy under Contract Number DE-AC03-76SF00098.

Properties of Heavy Quark Jets Produced by e^+e^- Annihilation at 29 GeV

Peter Cavanagh Rowson

ABSTRACT

The Mark II detector in the e^+e^- storage ring PEP at the Stanford Linear Accelerator Center (SLAC) is used to measure selected properties of hadronic events corresponding to produced bottom or charm quarks. Heavy flavor enrichment is accomplished by tagging events with prompt electrons or muons. Differences between bottom, charm and average jets are observed for momentum, transverse momentum, rapidity and jet mass distributions. A detailed study of the charged multiplicity of b- and c-enriched events finds the mean multiplicity of bottom and charm events to be $16.2 \pm 0.5 \pm 1.0$ and $13.2 \pm 0.5 \pm 0.9$ respectively, where the first error is statistical and the second is systematic. The corresponding 'non-leading' multiplicities of charged particles accompanying the pair of heavy hadrons are $5.2 \pm 0.5 \pm 0.9$ for bottom, and $8.0 \pm 0.5 \pm 0.9$ for charm. We find from these non-leading multiplicities that bottom and charm hadrons fragment with mean energy fractions of

$$< z >_b = 0.79^{+0.10}_{-0.05} \quad and \quad < z >_c = 0.60^{+0.09}_{-0.11}$$

These results confirm the expected hard fragmentation of heavy quarks and agree with previous measurements based on leptonic inclusive spectra and D^* fragmentation.

Acknowledgements

I would like to thank my advisor George Trilling for his guidance, humor and keen insight. I also thank Gerson Goldhaber for his always welcome advice. Other Berkeley professors to whom I owe a debt of thanks for wise counsel or fine instruction are Willy Chinowsky, Gene Commins, Bob Ely, Dave Jackson, and Mahiko Suzuki. I also thank Jonathan Dorfan of SLAC for support. Thanks are due to the entire Mark II collaboration for an excellent opportunity in Particle Physics. Most importantly I would like to thank my fellow graduate students, some from within the Mark II and some not, for companionship and for the best teaching I've seen during my time in school.

Table of Contents

Acknowledgements ii

Table of Contents iii

1. Introduction 1

1.1 Quark Fragmentation 4

1.2 The Weak Decays of Heavy Hadrons 6

1.3 Hadronic Final States in e^+e^- Annihilation 8

2. The Mark II Detector 11

2.1 Vertex Chamber 11

2.2 Main Drift Chamber 13

2.3 Time of Flight System 14

2.4 Magnet Coil 14

2.5 Liquid Argon Electromagnetic Calorimeter 14

2.6 Muon System 15

2.7 Small Angle Tagging System 16

2.8 Trigger System 17

3. Analysis 21

3.1 Monte Carlo Event Simulation 21

3.1.1 Quark Fragmentation 21

3.1.2 Weak Decays of Heavy Hadrons 23

3.1.3 Monte Carlo Bottom Hadron Decays 24

3.2 Hadronic Event Selection 27

3.3 Lepton Identification 29

3.4 Electron Identification 30

3.5 Muon Identification 34

3.6 Flavor Tagging with Leptons 36

3.7 Drift Chamber Performance 41

4. Properties of Heavy Quark Jets 45

4.1 The Simulation of Backgrounds 46

4.2 Momentum Distributions 50
4.3 Rapidity Distributions 50
4.4 Jet Invariant Mass 53
5. Properties of Heavy Quarks Events: Charged Particle Multiplicity 58
5.1 Multiplicity Unfold 59
5.2 Correcting for Non-uniform Data Quality 62
5.3 Background 64
5.4 Fit Results 67
5.5 Corrections 69
5.6 Results and Discussion 71
5.7 Systematic Errors 78
6. Conclusion 80
REFERENCES 81

1. Introduction

In e^+e^- annihilation at high energy several fundamental processes contribute to the interaction cross section. Among these is Bhabha scattering where the final state consists of an e^+e^- pair; the leading order Feynman diagrams are shown in Figures 1.0a and 1.0b. Muon and tau pair production proceed to first order via an annihilation diagram analogous to Figure 1.0a. In fact, the remarkable property of e^+e^- interactions is the potential to generate, via the annihilation mechanism, all pairs of charged particles for which the reaction is above threshold. The cross section for pair production of point-like fermions is given by

$$\sigma = \frac{4\pi\alpha^2 q^2}{3s}\beta(\frac{3-\beta^2}{2}) \tag{1}$$

where s is the square of the center of mass (c.m.) energy, β is the velocity and q is the charge of the produced particles and α is the fine structure constant.

The process studied in this thesis is the production of hadronic jets in e^+e^- annihilation, in particular heavy flavor (charm or bottom) hadronic jets. The basic underlying mechanism for this process, now supported by extensive experimental evidence, is the generation of quark-antiquark pairs by an intermediate virtual photon or neutral weak vector boson (Figure 1.0c). Since the threshold factor in equation 1 rapidly approaches one, at the PEP c.m. energy of $\sqrt{s} = 29$ GeV the relative cross sections for the production of all known quarks and leptons will be simply in proportion to their charges squared. The established quarks of the standard model are listed in Table 1.0.

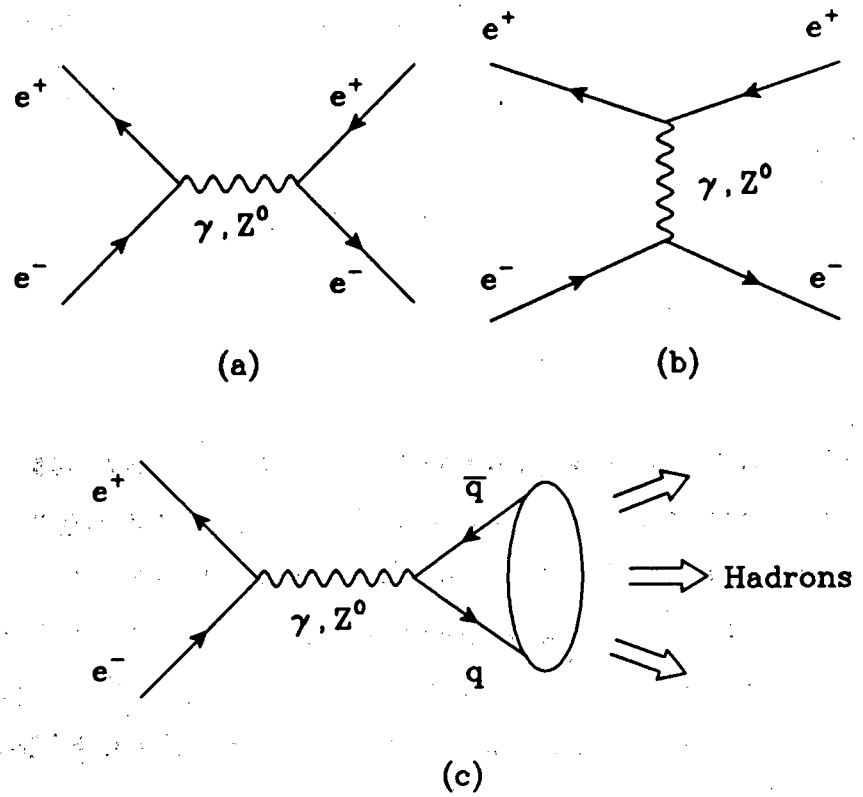

Figure 1.0: Lowest order contributions to Bhabha scattering and quark pair production.

Quark Flavors		
flavor	effective mass	charge
up (u)	0.3 GeV $/c^2$	+2/3
down (d)	0.3 GeV $/c^2$	-1/3
strange (s)	0.5 GeV $/c^2$	-1/3
charm (c)	1.5 GeV $/c^2$	+2/3
bottom (b)	5.0 GeV $/c^2$	-1/3

Table 1.0

According to this approximate model, the individual contributions to the hadronic rate due to up, down, strange, charm and bottom quarks are in the ratio 4:1:1:4:1. The heavy flavors charm and bottom therefore account for about 45% of

the hadronic cross section at PEP. Other interaction mechanisms can lead to final states with hadrons. These higher order interactions such as two photon processes and radiative Bhabha events where the radiated photon materializes as hadrons (Figure 1.1) will be shown to contribute the background in our hadronic event sample.

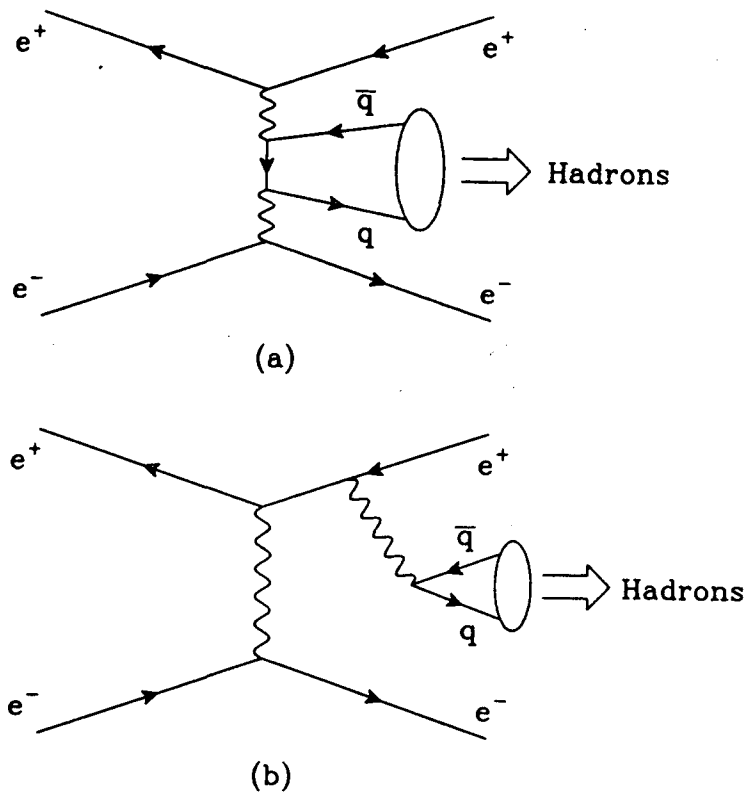

Figure 1.1: Second order processes.

The simple picture of point like production of quark pairs as the basis of hadronic production ignores the fact that quarks are not observed in isolation; their existence is inferred. Experimental evidence for quarks derives from the properties of the hadronic spectrum of mesons and baryons, deep inelastic lepton nucleon scattering and the existence of hadronic jets due to quark pair production in e^+e^- annihilation. It is confidently believed, though rigorous theoretical proof remains to to be found, that the Strong or Color Force confines quarks to within hadronic dimensions (≈ 1 Fermi).

For the case of quark pair production in e^+e^- annihilation, the particles that are actually observed in a detector derive from two types of processes:

i) quark fragmentation into hadrons,

ii) electroweak decays of hadrons.

The distinct characteristics of these two phenomena and their contributions to the measurement of jet properties will be a recurring theme for the remainder of this thesis. In what follows, the strong and electroweak processes in hadronic events will be discussed in turn.

1.1 Quark Fragmentation

The formation of hadrons from the hypothetical quark pair, a process alternatively known as hadronization or quark fragmentation, seems to be extremely complex and is far from understood. However, several elaborate phenomenological models exist that reproduce the main features of the data rather well when implemented in the Monte Carlo programs used in high energy experiments. We will describe some basic features of the strong interaction that are relevant to quark fragmentation in e^+e^- annihilation.

The strong interaction is presently understood in terms of the theory of Quantum Chromodynamics (QCD) [1]. QCD is a gauge theory, similar in most respects to the prototypical gauge theory, Quantum Electrodynamics (QED). QCD describes the interactions of quarks with the gauge bosons of the color force, known as gluons. The underlying symmetry group of QCD is non-abelian (color SU(3)); unlike the photons of QED, the gauge bosons of non-abelian theories must couple directly to each other. This fact, in conjunction with the strength of the strong coupling constant α_s, is responsible for the failure of perturbation theory in many QCD calculations. QCD perturbation theory can, however, give satisfactory results in the high momentum transfer regime. This is due to a property of a class of non-abelian gauge theories known as asymptotically free theories [2, 3]. In these theories the coupling constant is a *decreasing* function of the relevant interaction energy scale, in direct contrast to the diverging effective electric charge at small distances

in QED. As a result, quarks behave like free particles when probed at sufficiently small length scales. Asymptotic freedom helps explain why a point-like cross section is observed in e^+e^- annihilation hadronic production, and why the parton model for the interaction of point like objects within hadrons sucessfully describes deep inelastic lepton-nucleon scattering.

Quark fragmentation into hadrons is a relatively low energy non-perturbative QCD process and is most conveniently modeled by Monte Carlo techniques. The fragmentation models presently used by high energy physicists are numerous and will not be described here [4, 5, 6]. The event generator used in this analysis is one of a general class of independent fragmentation algorithms, named for the fact that jet to jet color interactions are neglected. In this model hadronization proceeds through a succession of fundamental processes of the form:

$$quark \rightarrow quark + meson$$

Our Monte Carlo has been modified to allow for the generation of baryons as well as mesons. The hadronic cascade divides the available energy into progressively smaller pieces, with a given cascade branch terminating when its free quark energy falls below the pion rest mass. The algorithm is schematically illustrated in Figure 1.2.

The primary $u\bar{u}$, $d\bar{d}$, $s\bar{s}$, $c\bar{c}$ or $b\bar{b}$ quarks, each with momentum p_0 are separately cascaded, a process in which each quark is coupled to a vacuum produced pair of $u\bar{u}$, $d\bar{d}$, or $s\bar{s}$ quarks. Due to their relatively large masses, vacuum pair production of the heavy flavors is negligible and may be ignored [7]. The primary quark and the secondary anti-quark combine to form a meson with momentum P_0, leaving momentum $p_1 = p_0 - P_0$ to the remaining free quark which then fragments in an analogous way. It is assumed that the distribution in fractional momenta $x = P_i/p_i$ at each step is independent of the total incoming quark momentum . A significant contribution to hadron production is due to the radiation of hard gluons from the initial quark pair. In our simple model, gluons are converted into a quark-antiquark pairs, and the quarks are then hadronized in the usual way.

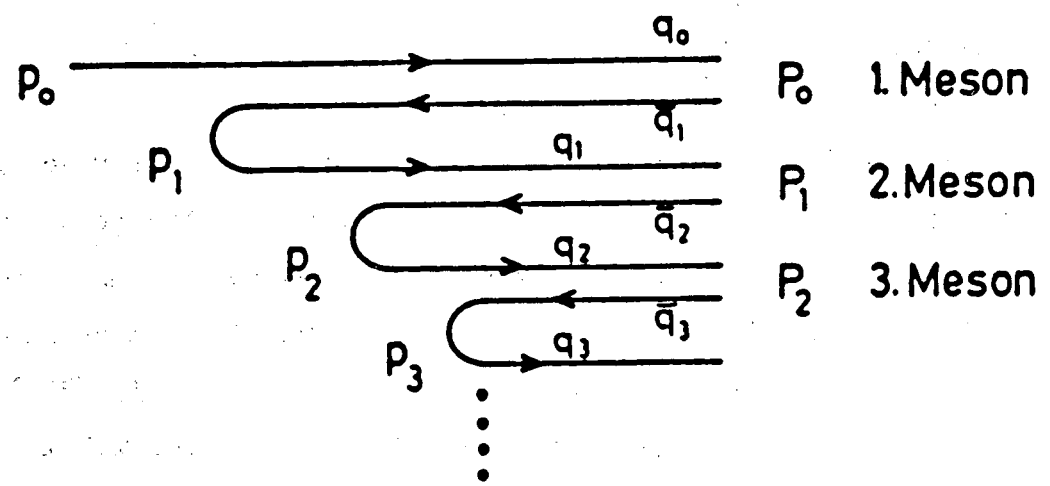

Figure 1.2: Hadronization in the Independent Fragmentation model.

1.2 The Weak Decays of Heavy Hadrons

The realm of the strong interaction extends to typically 10^{-22} seconds or so after the e^+e^- collision; the particles that survive beyond this point generally decay electromagnetically or weakly (notable exceptions are the vector meson states ϕ and ψ whose strong decays are dynamically supressed). In the case of $c\bar{c}$ or $b\bar{b}$ quark pair production, the produced heavy flavor states typically decay via the weak interaction after $10^{-13} - 10^{-12}$ seconds. The weak and electromagnetic interactions are well described by the SU(2) $\times$ U(1) gauge theory of Weinberg, Salam and Glashow [8, 9, 10]. In this model the chiral left-handed component of the fundamental fermions are grouped into weak iso-doublets, as shown below,

$$\begin{pmatrix} \nu_e \\ e \end{pmatrix} \begin{pmatrix} \nu_\mu \\ \mu \end{pmatrix} \begin{pmatrix} \nu_\tau \\ \tau \end{pmatrix} \begin{pmatrix} u \\ d' \end{pmatrix} \begin{pmatrix} c \\ s' \end{pmatrix} \begin{pmatrix} t \\ b' \end{pmatrix}$$

where the hypothetical top quark is predicted to complete the bottom quark dou-

blet. The first, and lightest, lepton and quark doublets given above are referred to as the first fermion generation: the electron and its neutrino, along with the up and down quarks. The second and third generations are grouped similarly. The standard model does not constrain the number of generations at all, but only requires the given arrangement into paired doublets. The right-handed components of each massive fermion are weak iso-singlets (right-handed neutrinos are absent). The quarks that appear in the weak doublets are not eigenstates of the strong interaction, since the weak interaction does not conserve flavor. The mixing matrix that describes these weak transitions is by convention defined so that the weak iso-doublet d',s' and b' quarks are each linear combinations of the down, strange and bottom eigenstates. This matrix, parameterized by Kobayashi-Maskawa (K-M) in terms of angles analogous to the well known Cabibbo angles of the four quark model [11] , has been relatively well determined by experiment [12]. The dominant weak decay chain is found to be $b \rightarrow c \rightarrow s \rightarrow u$. Bottom hadrons will almost always decay into charm hadrons, for which the K-M favored decay modes will include kaons, lambdas or other states with non-zero strangeness.

Table 1.1 lists the known heavy flavor states (with charge conjugate states not shown), where we have not included the hidden flavor $c\bar{c}$ or $b\bar{b}$ bound states. The semi-leptonic branching ratios are taken from the Particle Data Group booklet [13].

State	Mass (GeV/c^2)	Quark Content	Semi-leptonic B.R.
Charmed Hadrons			
D^+	1.869	$c\bar{d}$	0.190 (electrons)
D^o	1.865	$c\bar{u}$	0.053 (electrons)
D^{*+}	2.010	$c\bar{d}$	-
D^{*o}	2.007	$c\bar{u}$	-
F^+	1.971	$c\bar{s}$	(not measured)
F^{*+}	2.140	$c\bar{s}$	-
Λ_c^+	2.228	cud	0.045 (electrons)
Bottom Hadrons (B.R.s are for a B^+/B^o mix)			
B^+	5.271	$b\bar{u}$	0.130 (electrons)
B^o	5.274	$b\bar{d}$	0.124 (muons)
B^*	5.323	$b(\bar{u}$ or $\bar{d})$	(not measured)

Table 1.1

The best experimental information is available for the heavy flavor mesons, though much of what will be discussed below applies equally well to the baryons.

A simple model of the mechanism for heavy hadron weak decay is provided by muon decay (Figure 1.3a). Muon decay is a purely leptonic process, unlike the decay of a bottom or charm meson. However, the spectator model (Figure 1.3b), in which one quark of the hadron decays while the other is assummed to be uneffected, has been found to be useful as a first guess for lifetime calculations. The inadequacies of this model are however apparent in light of the fact that the lifetimes of the charged and neutral D-mesons differ by more than a factor of two, in contradiction with their expected equality. The ramifications of the spectator model, for the case of B-meson decay kinematics, are discussed in greater detail in Chapter 3.

1.3 Hadronic Final States in e^+e^- Annihilation

The properties of hadronic events produced in e^+e^- annihilation have generally been studied as averages over all flavors weighted by the relative flavor populations.

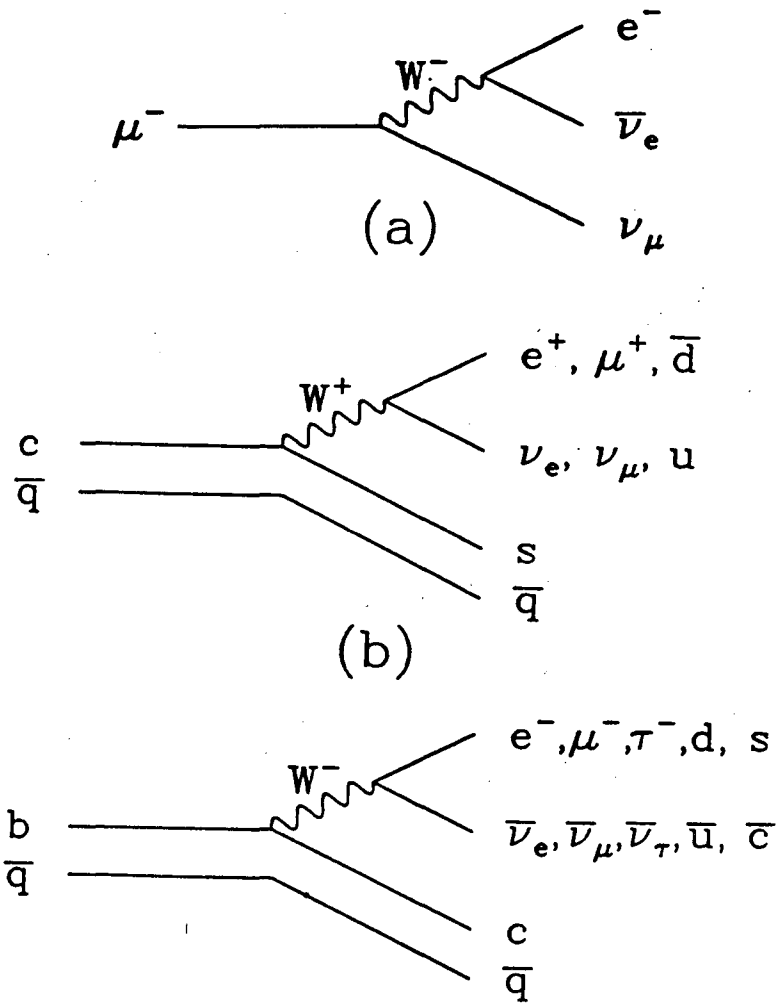

Figure 1.3: Weak decay: muon decay and spectator diagrams for meson decay.

There is little reason to assume much difference between hadronic jets from up,down and strange quarks, but for charm and especially bottom, the weak decay products as well as the heavy quark fragmentation properties play an important role. Consequently, the properties of the heavy quark jets may differ significantly from those of u, d and s jets. In this thesis, we will exploit the special properties of heavy flavor semi-leptonic decay and obtain a sample of hadronic events which is enriched in charm and bottom. By knowing the flavor composition of the enriched samples it will then be possible isolate the properties of charm and bottom jets. The lepton tagging method relies on the significant semi-leptonic decay branching ratios and relatively large masses and hence distinct decay kinematics of the heavy hadrons.

The high momentum, and in the case of bottom, large transverse momentum of the leptons due to c or b-decay, make relatively clean separation of these modes possible. The importance of reliable lepton identification to this analysis will be made clear at the onset.

Flavor dependent differences in the properties of hadronic jets may stem from either weak decay or hadronization processes. We will show how both of these phenomena contribute to the observed characteristics of bottom and charm jets. In $b\bar{b}$ events, a large proportion of the observed particles are due to weak decays. As a result, many of the properties of b-jets are determined by the characteristics of b-decay. To a lesser extent, the same is true for c-jets and c-decay. In light quark jets, weak decay processes play almost no role; the properties of u-, d- and s-jets are overwhelmingly determined by the initial hadronization.

The isolation of the properties of single flavor jets is of interest in its own right. In addition, the insight obtained from such studies may eventually serve to illuminate the now obscure question of the reason for the existence of several fermion generations.

2. The Mark II Detector

The Mark II was a general purpose magnetic spectrometer designed to detect the charged and neutral particles resulting from high energy e^+e^- annihilation [14, 15]. The detector's various components provided both particle tracking and electromagnetic calorimetry as well as limited particle identification capability. The Mark II was moved from the SPEAR e^+e^- storage ring and and installed in the larger PEP e^+e^- storage ring at the Stanford Linear Accelerator Center (SLAC) during the summer of 1979. A total of approximately 220 pb^{-1} of data at a center of mass energy of 29 GeV were collected at PEP by the end of the experiment in the spring of 1984. During the Mark II's tenure at PEP, several detector configurations were used. We will be concerned solely with the data obtained during the final stage that included a high resolution vertex detector and which represents the largest share (207 pb^{-1}) of the total integrated luminosity. The performance of the main drift chamber deteriorated during the fall of 1982, and while this problem was remedied by the following spring, care will be taken in this thesis to account for uneven data quality.

The Mark II was constructed with an overall cylindrical symmetry about the axis defined by the colliding electron and positron beams. In the section that follows, the detector's separate functional components will be described in the order in which they are encountered proceeding radially outward from the beamline (the z axis). The ends of the detector were instrumented with electromagnetic calorimeters, but since this thesis makes no use of these devices, they will not be described here. Two views of the Mark II detector are shown in Figures 2.0 and 2.1.

2.1 Vertex Chamber

The Vertex Chamber (VC) was a high resolution drift chamber designed to

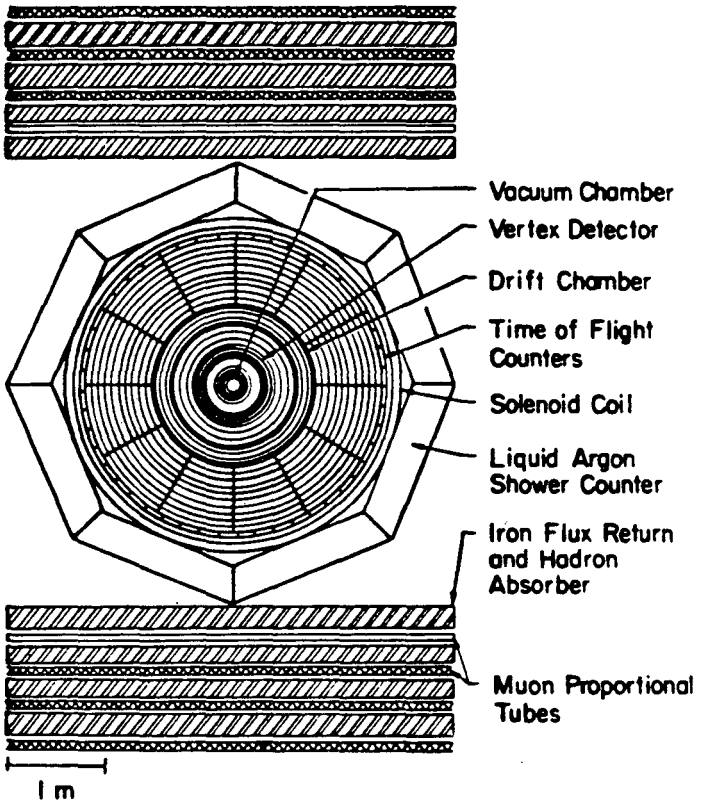

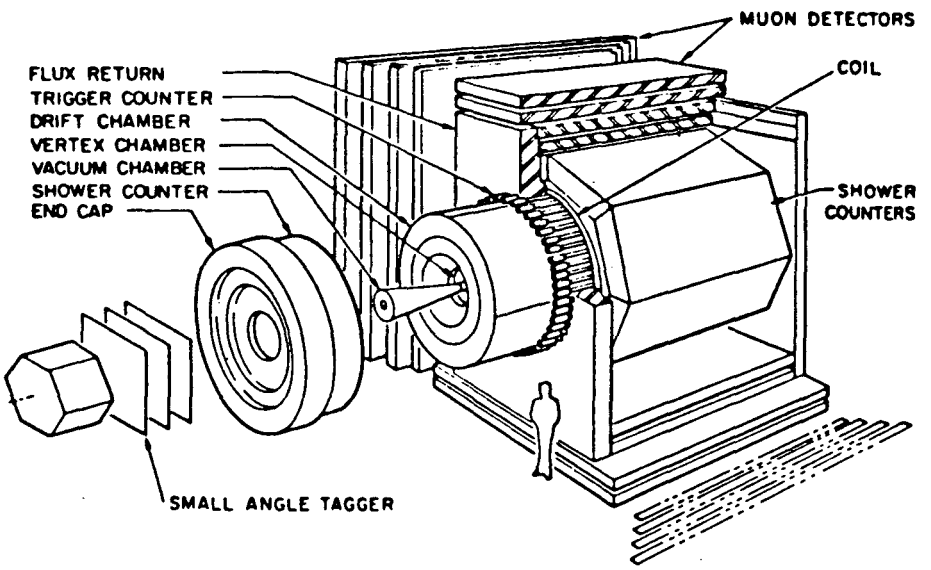

Figure 2.0 and 2.1: Cross sectional and isometric views of the Mark II detector.

reconstruct secondary vertices due to particle decays. This capability also allowed accurate extrapolation of tracks to the beam interaction point. The VC consisted of seven axial wire layers that were separated into two groups to optimize the extrapolation measurement: an inner band of four layers of $60-70$ sense wires at a mean radius of ≈ 10 cm, and a outer band of three layers of $180-190$ sense wires at a mean radius of ≈ 30 cm. The tracking data at small radii provided by the VC significantly improved the overall momentum resolution of the combined VC and Main Drift Chamber tracking system.

In order to minimize multiple coulomb scattering errors, the beam pipe doubled as the VC inner wall and was constructed from Beryllium, a low Z material. The 1.4 mm thick beam pipe totaled $\approx 0.6\%$ of a radiation length and had a radius of 7.8 cm. With a measured spatial resolution of about 100 μm per layer, the VC had an RMS error on extrapolation to the origin given by

$$\sigma_{ex}^2 = (95\ \mu\mathrm{m})^2 + \left(\frac{95\mu\mathrm{m}}{p}\right)^2 \tag{1}$$

where the second term is due to multiple scattering with momentum p measured in GeV/c. The vertex finding capabilities of the VC play a role in this thesis only insofar as they aid the detection of conversion pairs and Dalitz decays.

2.2 Main Drift Chamber

The Main Drift Chamber (DC) was the heart of the Mark II tracking system. Sixteen equally spaced concentric sense wire layers covering radii between 41 cm and 145 cm, were contained within a common gas volume. Six layers were axial, while the remaining ten were skewed at ± 3 deg to the beam axis to provide stereo information used to obtain a z position measurement. The spatial resolution per layer was typically 200 μm. With the nominal 2.35 kG magnetic field, the momentum resolution in the transverse plane was

$$\left(\frac{\delta p_{xy}}{p_{xy}}\right)^2 = (0.025)^2 + (0.011 p_{xy})^2 \tag{2}$$

where p_{xy} is in units of GeV/c, and the first term is due to the contribution of multiple scattering.

The momentum measurement provided by the DC is combined with information from the liquid argon calorimeter to identify electrons, and with muon system data to identify muons.

2.3 Time of Flight System

The Time of Flight (TOF) system surrounded the Main Drift Chamber gas can at a radius of 1.5 m and consisted of 48 longitudinal plastic scintillator strips, each 3.4 m long and instrumented at both ends with photomultiplier tubes. Both timing and pulse height information from each phototube pair were digitized and used to obtain a slewing corrected time of flight measurement for a track traversing the corresponding scintillator strip. The overall resolution of the TOF system for single hits was approximately 400 psec.

While useful for particle identification during the early days at SPEAR, in the high energy PEP environment, the TOF system was mainly relegated to use by the trigger system. The sole use of the TOF system in this thesis is the identification of low momentum electron candidates that may be members of photon conversion or Dalitz decay pairs.

2.4 Magnet Coil

The aluminum solenoidal magnet coil lay beyond the TOF system at a radius of 1.6 m. The coil was double layered, and water cooled through a conduit that ran inside the conductor. Originally, the magnet provided an axial magnetic field of 4.64 kG, but due to a short that developed between the inner and outer windings, only the outer conductor was powered during all but the first 3.4 pb^{-1} of the data collected for this analysis. With one solenoid loop, the nominal magnetic field was 2.35 kG, and was uniform to within 0.5% within the tracking volume. The coil thickness was 1.3 radiation lengths.

2.5 Liquid Argon Electromagnetic Calorimeter

The primary function of the Liquid Argon Electromagnetic Calorimeter system

(LA) was the detection of electromagnetic showers due to photons or electrons. The total solid angular coverage of the LA was about 64% of 4π. The eight LA modules encircled the magnet coil in an octagonal array, each module a self contained unit approximately 3.8 m long, 1.8 m wide, and 0.3 m thick. Within each module, separated by 3 mm and immersed in liquid argon, were 37 planes of 2 mm lead/antimony used for both signal collection and as a shower medium. The front of each module (the side closest to the magnet) was used for a trigger gap, consisting of three aluminum planes separated by 8 mm with the middle plane longitudinally segmented into 3.8 cm wide signal strips. The trigger gap was designed to identify showers that had originated in the magnet coil.

The lead readout planes were at high voltage and were arranged in strips: 'F' strips parallel to the beam line that measured azimuth (ϕ), 'T' strips perpendicular to the F strips for polar angle (θ) determination, and 'U' strips at 45 deg to the F and T directions for ambiguity resolution. Figure 2.2 schematically shows the alternating high voltage and ground planes, as well as the ganging pattern employed to reduce readout electronics while maximizing front to back shower information.

The total calorimeter thickness was $\approx$ 14.5 radiation lengths, with roughly 20% of the shower energy deposited in the liquid argon. The LA system achieved an overall RMS energy resolution of $\sigma(\mathrm{E})/\mathrm{E} = 12\%/\sqrt{E}$, with a spatial resolution for Bhabha electrons that allowed for the localization of the incident track to within $\sigma = 7$ mm. The LA system is essential to the electron identification algorithm discussed in chapter 3.

2.6 Muon System

Four muon walls surrounded the Mark II central detector: above, below and on both sides. Each wall consisted of four layers of steel hadron absorber alternating with layers of extruded aluminum proportional tubes . The first layer measured the polar angle, while the remaining three were oriented for azimuthal discrimination. The overall angular acceptance of the full system was only $\approx$ 45% of 4π, an unfortunate feature that limited the size of the muon event data sample. The muon

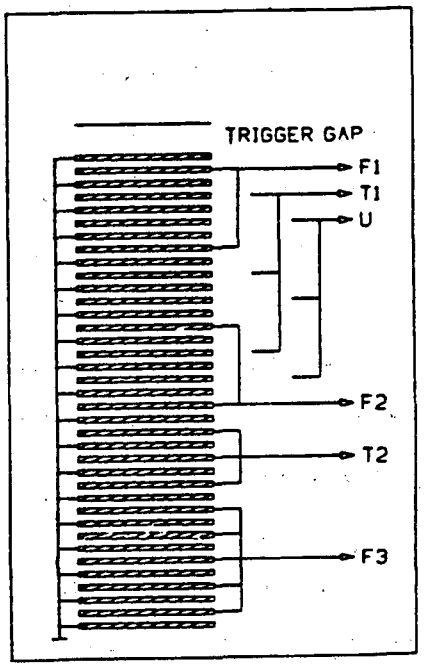

Figure 2.2: The Liquid Argon calorimeter readout ganging scheme.

system and the LA calorimeter account for about 7.4 interaction lengths; a muon typically requires a momentum of at least 1.8 GeV $/c$ to penetrate all four layers.

2.7 Small Angle Tagging System

A set of tracking and calorimetric devices were symmetrically placed at both ends of the Mark II, covering the angular region of 21 to 82 milliradians with respect to the beamline. The Small Angle Tagger (SAT) consisted of (proceeding outward along the beamline from the interaction point) 3 layers of planar drift chambers with a spatial resolution in the transverse plane of $\approx$ 300 μm per layer, 3 layers of acceptance defining scintillator, and a lead- scintillator shower counter consisting of $\approx$ 20 radiation lengths of 18 layers of alternating $\frac{1}{4}$ inch lead and

$\frac{1}{2}$ inch plastic scintillator capable of an energy resolution of $\sigma(\mathrm{E})/\mathrm{E} = 15\%/\sqrt{E}$. The system was designed to tag small angle Bhabha scattered electrons, as well as the scattered electrons due to two-photon interactions. The combination of the acceptance defining scintillator and the shower counters used Bhabha events to measure luminosity to a precision of about 5%.

2.8 Trigger System

The beam crossing rate at PEP of approximately 400 kHz, once every 2.4 μsec, necessitated a selective electronic trigger system [16]. The Mark II two-level trigger was able to hold the event acquisition rate to a few hertz. The principle employed combined a fast ($\approx$ 1 μsec) and relatively simple primary trigger, with a more sophisticated pattern recognizing secondary trigger that used data from the two drift chambers to find charged tracks. A Master Interrupt Controller (MIC) orchestrated the two-tiered system.

Various primary triggers were employed. The *Charged Trigger* required coincidence of a delayed beam crossing signal, a TOF hit signal and the satisfaction of a DC and VC layer hit pattern criterion. A programmable Memory Logic Module (MLM) stored the valid tracking system hit patterns; this pattern was changed at times if a particular layer ran at reduced efficiency. The *Neutral Trigger* fired if a threshold was exceeded in the front section of any two of the eight LA calorimeter modules, or if the total calorimetric energy deposit (including the Endcap proportional tube calorimeters) exceeded a higher threshold. A *Bhabha Trigger* used the SAT system to trigger on small angle Bhabha scattering events.

Following a primary trigger, the primary electronics sent a signal to MIC that in turn issued a WAIT flag halting data collection. The secondary trigger track finding cycle was initiated by a simultaneous START pulse from the primary trigger. The Master Clock (MC) received the START signal, sent a BUSY flag to MIC, and oversaw the operation of the trackfinding microprocessors at 10 MHz for 34 μsec. A deadtime of about 3% per kHz of primary trigger rate resulted from the MC cycle delay. The MIC received all secondary trigger data, from the trackfinding

electronics as well as from electronics associated with detector components other than the drift chambers, and arbitrated the final trigger decision.

The criteria used by MIC for selecting events to be logged were easily programmable on-line, and several trigger formats were used during the experiment to accomodate short term hardware problems, PEP running conditions and test modes using cosmic rays. If a secondary trigger passed, MIC would interrupt the Mark II Vax 11/780 computer to initiate data transfer and subsequent logging to tape. The process was completed by MIC, whether or not a secondary trigger had occurred, by the lifting of the WAIT flag, and a system RESET.

A selected subset of twelve of the twenty four logical ORS from all of the tracking layers plus the TOF system were available to the secondary trigger, and were used to define two types of legal tracks:

1. A-tracks, those passing through the entire tracking system, required typically 2 of 4 inner VC layers hit, 4 of 8 selected DC layers hit where 2 of these 4 hits were in the outer 6 DC layers, and a TOF hit.
2. More steeply dipped tracks were called B-tracks, and usually only required 3 of 4 inner VC hits.

These two track categories are not mutually exclusive; most A-tracks also satisfy the B-track requirements.

The layers included in the trigger were changed occasionally: the outermost layer was removed from the trigger when its efficiency was seen to deteriorate, and during periods of high PEP beam noise it was sometimes necessary to remove a few inner VC layers to reduce excessive trigger rates.

The principle behind the operation of the secondary trigger track finding was the mapping of the twelve trigger layers into shift registers which were then fed into specialized coincidence modules called Curvature Modules. A device known as the Test and Pickoff Module transferred the tracking chamber shift register bits onto a dedicated trigger system bus. Twenty four programmable Curvature Modules were tied to this dataway, to allow for two sets of twelve different coincidence masks, one for each sign (clockwise or counterclockwise) of track curvature. The Master

Clock provided 10 MHz clock pulses that served to rotate each shift register layer at a constant angular speed while the 24 Curvature Modules operated in parallel. Figure 2.3 shows schematically how the programmable Curvature Module delays d_i and widths w_i enabled the system to find curved tracks. Track Counters were used to tally the the results of the search, and to forward these results to MIC for a final secondary trigger decision. A block diagram of the track finding system is given in Figure 2.4.

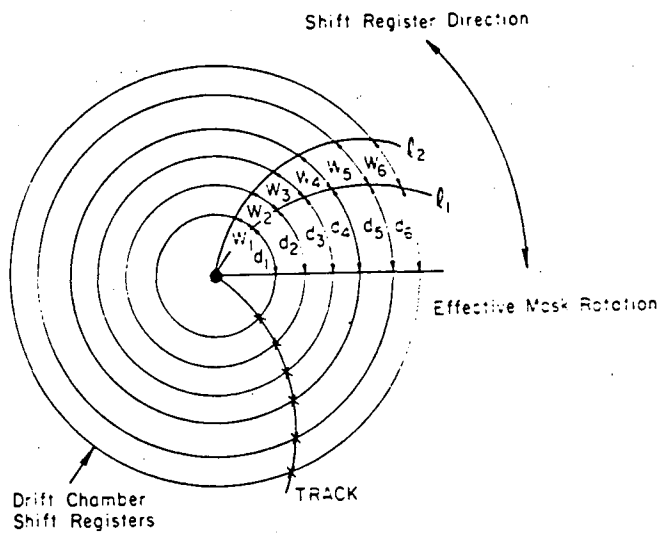

Figure 2.3: Track mask 'delays' d_i and 'widths' w_i.

The secondary charged trigger was typically satisfied if at least one A track and at least two tracks which satisfy the B track criteria were found by the pattern recognition hardware. Two A tracks will almost always satisfy this requirement. Valid neutral triggers were the TED (Total Energy Deposit) trigger which required at least 1 GeV of energy in the front section of at least two of the eight LA calorimeter modules, and the SED (Single Energy Deposit) trigger which was satisfied if the

total calorimetric energy exceeded 4 GeV. The Bhabha trigger was scaled by a factor of 16 due to the high rates for this trigger mode. The resulting secondary trigger rate rarely exceeded 4 Hz.

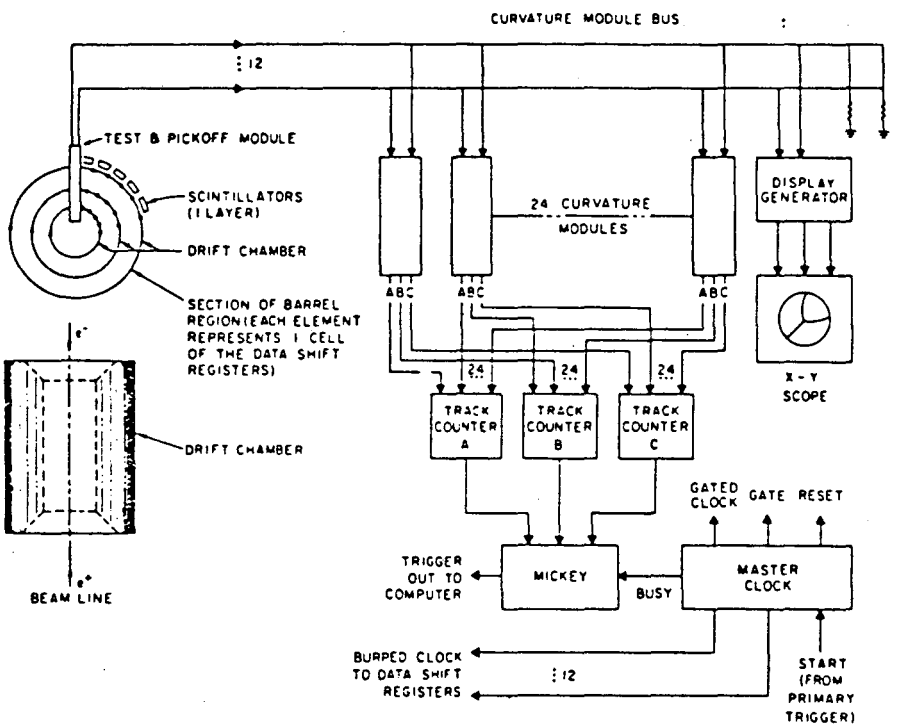

Figure 2.4: Block diagram of the secondary trigger system.

3. Analysis

Monte Carlo event simulation is crucial to this thesis for two reasons. Firstly, and most importantly, the Monte Carlo is used to evaluate efficiencies by modeling effects due to the Mark II apparatus. Secondly, the Monte Carlo provides quantitative distributions to compare with observations. In the first half of this chapter, we will describe a few features of the Mark II Monte Carlo event generator that are relevant to our measurements. This will be followed by a discussion of the preliminary stages of our data analysis.

3.1 Monte Carlo Event Simulation

3.1.1 Quark Fragmentation

In the introductory chapter we described a simple model of quark fragmentation, known as the Independent Fragmentation model, that is used by the Mark II Monte Carlo event generating program. More sophisticated fragmentation models exist, but the details of these models will not concern us here. All of the Monte Carlo models include a procedure for dividing the primary quark energies among the resulting hadrons. The procedure used by our Monte Carlo models this process using a *fragmentation function*. The fragmentation function determines the fraction of a propagating quark's energy that is imparted to the hadron eventually formed from the quark. Our fragmentation functions are parameterized in terms of this energy fraction $z \equiv E_{hadron}/E_{quark}$. Simple kinematical arguments indicate that light flavor hadrons fragment with a smaller energy fraction than do the more massive charm and bottom hadrons [17, 18]; two different forms for the fragmentation function are used:

$$f(z) \sim (1-z)^r \qquad r = 0.7 \text{ for u, d and s quarks}$$

$$f(z) \sim \frac{1}{z}\frac{1}{(1-1/z-\frac{\epsilon}{1-z})^2} \qquad \epsilon = 0.3 \text{ for c quarks and .03 for b quarks.}$$

The heavy quark fragmentation function is due to Peterson *et.al.* [19]. Figure 3.0 shows the light and heavy quark fragmentation functions given above.

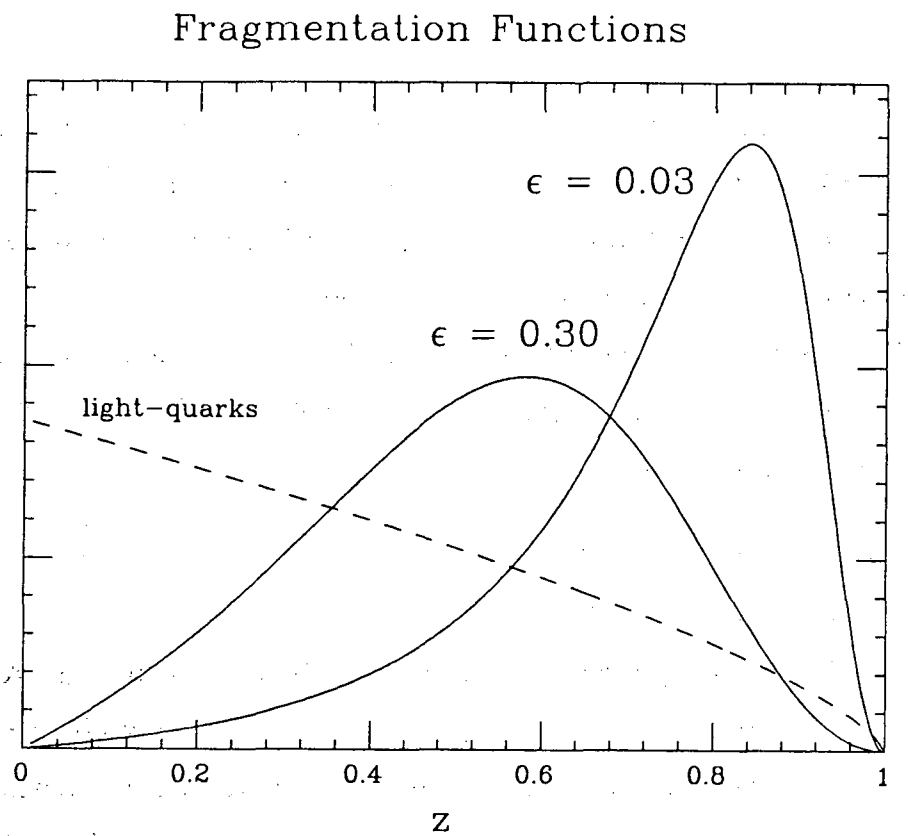

Figure 3.0: Fragmentation functions for bottom ($\epsilon = 0.03$), charm ($\epsilon = 0.3$) and light quarks ($r = 0.7$).

The choices of r and ϵ in the above formulation results in mean z values of 0.2,0.6 and 0.8 for light, charm and bottom quarks respectively, in agreement with observation: evidence for the hard fragmentation of heavy quarks has been observed in the momentum spectra of both the charmed mesons and the leptons due to semi-leptonic decay of charm and bottom hadrons [20]. In chapter 5 of this thesis the issue of fragmentation is independently addressed by an analysis of the charged multiplicity in heavy flavor events.

The Monte Carlo includes the contribution due to gluon radiative events that result in final state three and four hadron-jet topologies. Additional parameters in the Monte Carlo event generator include the light quark vector meson fraction (0.58) and the RMS p_T with respect to the initial quark direction for fragmenting quarks in jets (300 MeV/c). For the charmed and bottom mesons, the vector meson fractions are 0.75 and 0.50 respectively. In order to agree with observed strange particle generation in hadronic events, the Monte Carlo is adjusted to make strange quarks 20% of the total vacuum pair population, the other 80% going equally into u and d quark pairs. The Mark II event generator is described in greater detail in the thesis of H. Schellman [21].

3.1.2 Weak Decays of Heavy Hadrons

The Monte Carlo program used in this thesis approximates what is presently known about charm and bottom meson decay modes. No heavy flavor baryons are included in the Monte Carlo. The charmed mesons are the D and F with decay properties shown in Table 3.0. The entries in Table 3.0 are not identical to those given in the Particle Data booklet (see Table 1.1).

	semi-leptonic B.R.	hadronic modes
D^+	0.289	statistical isospin model with
D^o	0.106	resonant decays included
F^+	Not included. The purely leptonic decay to $\tau\ \bar{\nu}_\tau$ occurs with a B.R. of 0.15.	(see next subsection)

Table 3.0 : Monte Carlo charmed meson decays.

By virtue of the small contribution (20% of the charm mesons) due to F mesons and to their similarity to the D mesons, the exclusion of the F meson semileptonic decay modes has little effect when comparing data and Monte Carlo. The bottom mesons included are B_u, B_d and B_s.

	semi-leptonic B.R.	hadronic modes
B_u	0.12 for e and μ, 0.03 for τ	
B_d	same	(see next subsection)
B_s^o	0.13 for e and μ, 0.04 for τ	

Table 3.1 : Monte Carlo bottom meson decays.

The kinematics of all charmed hadron decays and bottom hadron semi- leptonic decays are done according to phase space, followed by *ad hoc* parameter tuning if this is necessay to better match experimental momentum spectra. Of particular importance to this analysis are the momentum spectra of leptons due to heavy quark semi-leptonic decay; the generated rest frame momentum spectra of prompt leptons for both bottom and charm decay are adjusted to agree well with measurements from DELCO (electrons due to D-mesons from ψ'' decay at SPEAR) [22] and CLEO (electrons due to B-mesons from $\Upsilon(4s)$ decay at CESR) [23]. In the case of hadronic b-decay, a more elaborate procedure was necessary, as will be described below.

3.1.3 *Monte Carlo Bottom Hadron Decays*

We will here summarize a few important parameters of b-hadron decay as implemented in the Mark II Monte Carlo . The Monte Carlo branching ratios for the various $B \rightarrow D + n\pi$ hadronic modes are handled in accordance with the Statistical Isospin Model [24]. The kinematics were originally determined entirely by phase space, but recent data from CESR indicates that this approximation is inadequate [23].

From the CLEO collaboration two basic facts concerning hadronic B-decay have emerged; the charged multiplicity is high, 6.0 ± 0.3, and the momentum spectrum of secondary D^o's is hard, much more like a semi-leptonic decay spectrum than a multi-body phase space spectrum [25]. These two observations have been incorporated into the Monte Carlo for both B and B_s hadronic decay.

The hadronic branching fractions within the Statistical Isospin model are determined as follows. The distribution of n in the decay $B \rightarrow D + n\pi$ is assummed to be

Poisson, where we treat the mean $\bar{n}$ as an adjustable parameter. For a given value of n, the distribution of BR's to the various allowed pion charge states is given by isospin Clebsch-Gordan coefficients. The values for $\bar{n}$ used in the B and B_s decay routines are adjusted so that the produced multiplicities are in agreement with the CLEO B decay multiplicity data. In Chapter 5 we will describe a measurement of the charged multiplicity of hadronic events due to $b\bar{b}$ quark production. Our readjusted Monte Carlo also agrees with these measurements.

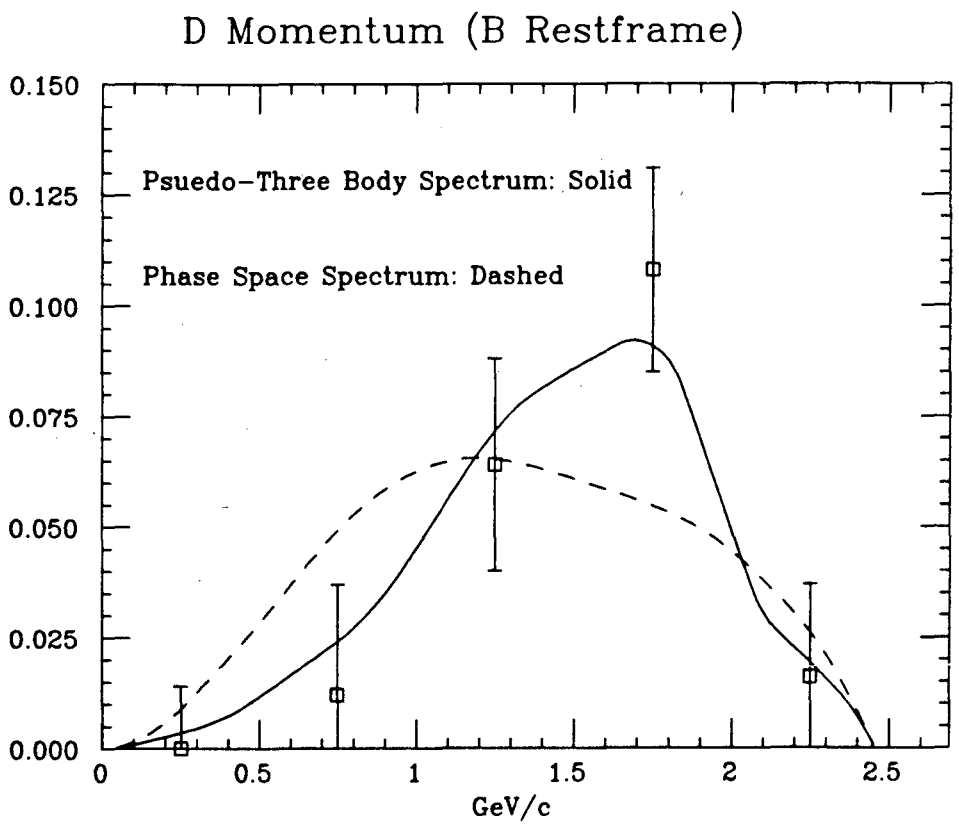

Figure 3.1: The D meson momentum spectrum from B decay. The solid line shows the result for the effective three body Monte Carlo model, the dashed line shows the phase space prediction and the data are due to the CLEO collaboration.

The spectrum of D mesons due to B decay is found to differ from the spectrum expected from a simple phase space model (Figure 3.1). To improve the decay kinematics, one needs to appeal to a model of the dynamics. The spectator diagram (Figure 1.3b) models the weak decay, and for semi-leptonic modes this model is all that is needed to determine the final state momentum spectra. For a hadronic decay, one must approximate the effects of the color force. The quark pair due to the decay of the W boson, and the pair of quarks consisting of the charm quark and the spectator quark, are each separately produced as color singlet objects. Naive color counting arguments predict the suppression of strong interactions leading to re-grouping of the color singlet quark pairs. For example, a suppressed configuration would form one color singlet from the c quark and the W-decay anti-quark. Therefore, to a good approximation one may separate the decay into two stages: an initial free quark process, followed by hadronization (Figure 3.2). It is the free quark stage that determines the D meson spectrum, yielding a spectrum typical of a three body decay. This scheme is implemented as follows:

1. The B meson is decayed into a D (or D^*) meson and two pseudo-quark jets, each of mass 800 MeV$/c^2$.
2. The pions are generated by decaying the recoiling two jet system according to phase space.

The D momentum spectrum is shown in Figure 3.1 along with the phase space spectrum and the CLEO data for D^o's (these plots include the contributions from S.L. decay) [23]The F momentum spectra for B_s decay are similar. For the purposes of comparison, D's due to D^* decay are not included in these plots. Our improved model fits the B-decay data well, and will be used in Chapter 4 to compare with measured properties of bottom jets.

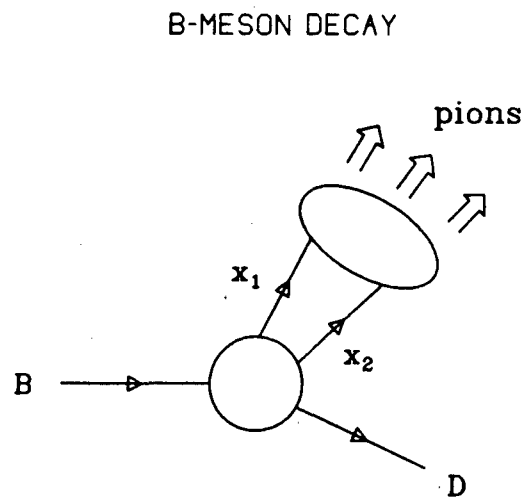

Figure 3.2: Pseudo-three body B meson decay.

3.2 Hadronic Event Selection

Since our interest is with the hadronic production process discussed in Chapter 1, we need to separate these so-called hadronic events in our data sample from those events due to Bhabha scattering, lepton pair production ($\mu^+\mu^-$ and especially $\tau^+\tau^-$) and higher order processes such as two photon interactions. We also need to eliminate background noise due to cosmic rays and beam gas collisions. During the course of the Mark II experiment at PEP, a standard set of hadronic event selection criteria have been developed that is both efficient and discriminating. The recognition of Bhabha, μ pair and cosmic ray events is generally trivial due to their charateristic low particle multiplicities. Tau lepton pair production and two photon hadronic production can, however, mimic the high multiplicity expected from hadronic events. The following cuts are designed to remove these backgrounds, and to select well-measured events.

1. The radial and longitudinal distances R_{vertex} and Z_{vertex} of the reconstructed event vertex from the average beam-beam interaction point must be less than 4 cm and 7 cm respectively. The RMS size of the luminous region is approximately $480\mu m$ in x, 60μm in y and 1.5 cm in z. The center of the luminous region is mainly determined with hadronic and Bhabha events. These loose cuts eliminate much of the beam gas background while removing very few good tracks.
2. Both charged tracks and neutral energy showers are selected by the following criteria.

Charged tracks:

i) The distances of closest approach to the center of the luminous region, R_{DCA} and Z_{DCA}, must be less than 4 cm and 8 cm respectively.

ii) The measured momenta p must be within the range 100 MeV $/c$ $<$ p $<$ 16 GeV $/c$.

iii) In order to assure that each track is within the high efficiency volume of the main drift chamber, $|\cos\theta_{track}|$ must be $\leq$ 0.7, where θ is the polar angle.

Neutral tracks:

i) The LA shower energy must be above 200 MeV.

ii) The percentage of LA shower energy shared with other showers in the event must be less than 50%.

iii) The closest approach of a charged track to the shower center must be greater than 7 cm (or, approximately, two lead strip widths) to prevent false signals due to overlap.

The event is then further constrained:

3. The total observed energy E_{total}, including both charged and neutral contributions, must equal or exceed 25% of E_{cm}, or 7.25 GeV at our E_{cm} of 29 GeV. Two-photon events, much of whose energy is carried by the forward scattered electrons and positrons that are not seen in the central detector, are eliminated by this cut.

4. To enrich our hadronic data sample with particularly well contained events, we demand that the event thrust axis , determined using both charged and neutral tracks, points into the high efficiency volume of the central detector. Thrust will be defined below. The requirement is that $|\cos\theta_{thrust}| \leq 0.5$, where θ_{thrust} is the polar angle of the thrust axis.
5. An important charged multiplicity cut requiring at least 5 charged tracks (excepting e^+e^- pairs due to conversions or π^o Dalitz decays), indispensible for the exclusion of $\tau^+\tau^-$ and Bhabha events, as well as a general basis for the exclusion of all types of background, is applied *after* the lepton selection process described below. Postponing this cut avoids biasing the multiplicity unfold procedure described later.

Given a set of 4-vectors in an event, the thrust axis is defined as the direction along which total projected momentum is a maximum. The scalar thrust is defined by

$$\mathrm{T} = \max_{\mathrm{T}}\left(\frac{\Sigma|\mathrm{p}_{\|}|}{\Sigma|\mathrm{p}|}\right)$$

(where the **T** axis is the axis that maximizes thrust). The thrust axis generally reflects the initial quark direction in hadronic events; according to our Monte Carlo, the angle between the thrust axis and the produced primary quark direction in hadronic events is less than 25 degrees about 80% of the time. In this thesis we will refer to the *event thrust*, calculated using all acceptable charged and neutral tracks in the event, and the *jet thrust* found from a subset of vectors belonging to a single jet in the event.

3.3 Lepton Identification

An algorithm for the identification of prompt electrons and muons has been developed for Mark II data analysis, and is described in detail in the thesis of M. Nelson [26]. For our purposes, prompt leptons are those leptons due to the decays of short lived heavy flavor states. Here we will outline this procedure and discuss both its efficiency for leptons originating in heavy quark decays, and its rate for misidentification.

3.4 Electron Identification

A distinguishing feature of the electron is its relatively small mass, some two hundred times smaller that the next most massive object, the muon. This fact turns out to be crucial in determining the special nature of the electron's electromagnetic interactions in matter. Above an energy threshold that varies for different materials (7 MeV in Lead), electrons lose energy in matter primarily by the generation of an electromagnetic shower. A shower occurs when an electron travelling through matter radiates photons of sufficient energy to place them in the regime where e^+e^- pair production is the dominant QED interaction process. The created electrons and positrons radiate in turn, generating a multiplicative process that only tapers off when typical radiated photon energies are low enough for ionization energy loss to dominate over radiation. The crux of this sequence of events is the process of radiation from accelerated charged particles, or bremsstrahlung. Bremsstrahlung occurs in inverse proportion to the square of the mass of the radiating particle, and is therefore suppressed relative to the electron rate by a factor of $(\frac{m_e}{m})^2$ for a particle of mass m, a factor of $O(10^{-4})$ for muons.

The Mark II LA calorimeter is designed to contain the high energy electromagnetic showers expected from electrons with energies up to the full beam energy of 14.5 GeV. The ratio $\frac{\mathrm{E}}{\mathrm{p}}$, where E is the measured energy and p is the momentum determined by the drift chambers, tends to be of order one for electrons produced within the barrel calorimeter acceptance, and much smaller for other charged particles such as muons, pions, kaons and protons. The hadrons do, however, interact strongly in matter and can lose a large fraction of their incident energy in hadronic cascades. Due to the fact that the interaction length in lead is $\approx$ 17 cm, considerably longer than the radiation length of $\approx$ 0.6 cm, hadronic cascades are morphologically distinct from electromagnetic showers; they tend to start from a point deeper into the calorimeter, and generally have a broader transverse structure. The electron selection algorithm we use does not rely on the observation of the full electron energy, but rather on a combination of energy deposition and shower geometry information within a small signal region defined relative to the incident charged track. In

this way, we minimize complications due to both the finite energy resolution of the calorimeters and possible confusion in determining energy sharing in multi-track events. Briefly, the electron identification algorithm proceeds as follows:

1. Tracking system information is used to extrapolate the path of an incident charged particle through the LA module.
2. A circular search region around the projected path is defined for selected ganged strips in the module and is expected to contain $\approx 80 - 90\%$ of the shower energy.
3. The deposited energies E_{F1+F2}, E_{T1} and E_U for the designated strip groups are then determined (see fig. 2.2). E_{front} is defined as the sum of the three group energies E_{F1+F2}, E_{T1} and E_U.
4. One then defines the quantity

$$E_{min} = \text{minimum}\left(\frac{E_{F1+F2}}{\alpha_F}, \frac{E_{T1}}{\alpha_T}, \frac{E_U}{\alpha_U}, \frac{E_{front}}{\alpha_{front}}\right)$$

where the α's are chosen such that $E > \alpha p$ for most ($> 70\%$) electrons. $\frac{E_{min}}{p}$ is required to be greater than 1.1 for electron candidates.

The efficiency of the electron finding algorithm for electrons within the fiducial volume varies from $\approx 90\%$ for electrons with momenta greater than 2 GeV, to $\approx 75 - 80\%$ for lower energy electrons. The range of efficiencies for electrons reflects a slight dependence on transverse momentum p_T where p_T is taken with respect to the event thrust axis. Small p_T electrons tend to be closer to the core of the hadronic jet where energy overlap in the calorimeter increases the energy assigned to the candidate track. Due to the good efficiency of our algorithm, the overall efficiency for finding electron events is dominated by the effects of our limited fiducial calorimeter acceptance of 64% of 4π.

The background in the electron sample is mainly due to misidentified hadrons. Even though the misidentification probability for a single pion is typically a fraction of a percent, the overwhelming preponderance of pions relative to electrons in our data results in background contributions to our lepton event data sample of $\approx 20 - 40\%$, depending on the mean p and p_T of the candidate tracks. Hadrons

can simulate electrons in either of two ways: by depositing energy due to nuclear interactions or by being assigned overlap energy due to nearby tracks or photons in a crowded jet, where in both cases the pattern of energy deposition satisfies the electromagnetic shower recognition criteria. Charge exchange reactions of the form

$$\pi^- + \mathrm{p} \rightarrow \pi^\circ + \mathrm{n} \quad \text{or} \quad \pi^+ + \mathrm{n} \rightarrow \pi^\circ + \mathrm{p}$$

are the dominant contributing process to the interacting hadron background, for the generated π^o's decay to photons that then shower electromagnetically.

Pion misidentification was investigated in reference 26 using Mark II SPEAR data on hadronic ψ decays to $2(\pi^+\pi^-)\pi^o$ and pion beam test studies at 2 GeV and 4 GeV made with one module of the LA calorimeter. The pions from ψ decay data covered the momentum range from 0.5 to 1.3 GeV $/c$, and therefore complemented the test beam data. Two reliable pion samples collected at PEP were also employed in this study: pions from $K_s^o \rightarrow \pi^+\pi^-$ and pions from three pion decays in $\tau^+\tau^-$ events. The PEP data were used to measure misidentification for pions with momenta from 2 to over 10 GeV $/c$.

The contribution of energy overlap to the background was determined in reference 26 by manipulating hadronic event data to simulate the process of false energy assignment to tracks in dense hadron jets. Tracks in jets were flipped 180 degrees from one jet to the opposite jet, and the flipped track was then subjected to the electron search algorithm. The end result of all this careful analysis is summarized in Table 3.2, which gives the hadron misidentification probabilities, binned by p and p_T, and combining both energy overlap and hadronic interaction effects [26]. (Note: The bin labels used below refer to the low bin edge. The highest p and p_T bins will by convention extend to include all data above the low bin edge.)

Background: electrons				
p/p_T (GeV/c)	0.0	0.5	1.0	1.5
1.0	0.023	0.010	0.007	0.007
2.0	0.015	0.008	0.007	0.007
3.0	0.010	0.006	0.005	0.005
4.0	0.007	0.005	0.004	0.004
5.0	0.007	0.005	0.004	0.004
6.0	0.006	0.004	0.003	0.003

Table 3.2 : Electron misidentification probabilities.

An additional, smaller source of background is due to electrons from unidentified pair conversions and Dalitz decays. With a prompt electron candidate in hand, a pairfinding program determines if the candidate is a member of a pair with efficiency given in Table 3.3 [26], where the method used by our pairfinding algorithm combines geometrical selection and electron identification. Each electron candidate is paired with oppositely charged tracks in the event and cuts are made on three properties of each pair:

1. The projected distance between the tracks in the transverse plane, at the point where the transverse projections of the tracks are parallel, must be less than 15 mm.
2. The distance between the tracks at the origin, in the z direction, must be less than 10 cm.
3. The track to track difference in dip angle must be less than 120 mrad.

If a pair satisfies the above criteria, the partner of the electron candidate is subjected to relatively loose electron selection tests. If the track momentum is less than 2 GeV /c, TOF information is used to require that the track time of flight be within 3σ of the time of flight expected for an electron. Tracks with momenta greater than 0.7 GeV /c are subjected to the electron shower recognition algorithm with $\frac{E_{min}}{p}$ required to be greater than 0.5. The rate for identifying false pairs for this

pairfinder is small, about 2%, mainly due to the method of electron identification used for both members of the pair candidate. The background due to missed pair electrons is typically $\approx$ 20% of the total background in a given p,p_T bin. The pairfinder efficiencies for identifying a real pair given an initial prompt electron candidate are given in Table 3.1.

Pairfinder Efficiency			
p/p_T (GeV/c)	0.0	0.5	1.0
1.0	0.762	0.793	0.714
2.0	0.734	0.786	0.800
3.0	0.718	0.800	0.735

Table 3.3 : Pairfinder efficiencies.

3.5 Muon Identification

As pointed out in the previous section, due to their small bremsstrahlung cross section muons do not produce electromagnetic showers. Instead, muons with momenta of more than a few hundred MeV/c lose energy uniformly along their trajectories by ionization processes. Charged hadrons have similar electromagnetic $\frac{dE}{dx}$ properties, but they also undergo nuclear interactions that result in rapid energy dissipation via hadronic cascades. Muons are in fact the most penetrating of all charged particles; a suitably designed absorber system will stop all other tracks.

Muons lose about 200 MeV per interaction length ($\approx$ 17 cm in iron), and therefore the momentum threshold for muon penetration of the full 7.4 interaction lengths of the muon system is just under 2 GeV. In this analysis, muon candidates are constrained by fiducial criteria that require the extrapolated muon momenta to be within the angular acceptance of the muon system, and to be of sufficient magnitude to penetrate all four steel walls. The implementation of muon candidate selection is a two step process. First, each drift chamber track within the fiducial volume is extrapolated through the muon system, and a search for proportional tube signals within a radius of two times the extrapolation error is made for each

of the four muons layers. The extrapolation error is estimated by combining the drift chamber tracking error ($\approx$ 3 cm) in quadrature with the calculated multiple coulomb scattering error (typically $<$ 10 cm). A muon candidate is then defined as a track with associated muon system hits in all four layers.

The geometrical acceptance of the muon system of 45% is the overwhelming factor in determining the efficiency of our muon recognition program. For muons *within* the fiducial volume, the efficiency is high, ranging from $\approx$ 80% for muons with momenta of $2-3$ GeV $/c$, up to over 90% for high energy muons (≥ 6 GeV $/c$). Inefficiencies are due to range straggling, multiple scattering losses and drift chamber track extrapolation errors that can place tracks outside of the 2σ search region, and to tube inefficiencies of about 3% per track per muon system layer.

Contributions to the muon background due to hadron misidentification are caused by hadron punchthrough, track overlap in the muon system and muon system noise. Noise was investigated by examining the muon system signal in data without any penetrating tracks, i.e. Bhabha events. It was found that the noisiest level, level 4, typically contributes a random hit for about 5% of the tracks in the fiducial volume. No tracks due entirely to noise are expected, but hadrons that penetrate to three levels may find their way into the muon sample due to a random hit in level four (this would occur for approximately 1 in every 2000 pions with at least 2 GeV $/c$). Track overlap background was simulated in much the same way as was done for the electron sample. A track flipping procedure was used to estimate the effect that associates muon system hits due to neighboring penetrating particles with a given extrapolated drift chamber track. Punchthrough probabilities for tracks within the fiducial volume for the first three muon system layers were determined from the muon system data, and then this information was extrapolated to yield the level four penetration rate. Pion punchtrough for the momentum range $2-10$ GeV $/c$ was examined using known pion sources: K_s^o decay, τ to 3π decay and charmed D^o meson decay to π K. The D^o data were also used to show that kaon and pion punchthrough rates are comparable.

There is also a contribution to the background due to non-prompt muons from

pion and kaon decay. The Monte Carlo was used to determine the size of this effect, which turns out to be a slightly larger component of the background than are the misidentified hadrons. The combined non-prompt and misidentification probabilities, binned by p and p_T, are given in Table 3.4.

Background: muons				
p/p_T (GeV/c)	0.0	0.5	1.0	1.5
2.0	0.0067	0.0064	0.0093	0.0101
3.0	0.0079	0.0082	0.0126	0.0075
4.0	0.0075	0.0066	0.0124	0.0115
5.0	0.0082	0.0100	0.0082	0.0108
6.0	0.0080	0.0073	0.0081	0.0073

Table 3.4 : Muon misidentification probabilities.

3.6 Flavor Tagging with Leptons

Due to the relatively large semi-leptonic branching ratios of the heavy quark hadrons, and to their hard fragmentation, a sample of events enriched in bottom and charm states can be obtained by requiring that each event contain a high momentum lepton [27]. The bottom and charm events can then be separated by exploiting the larger mass of b-hadrons; leptons due to b-decay will have relatively large transverse momenta with respect to the primary quark direction or jet axis. In practice, one determines p_T with respect to the event thrust or sphericity axis. Figure 3.3 shows the calculated transverse momentum spectra for leptons due to to various b and c-decays [28]. By applying a cut at a lepton p_T of ≈ 1 GeV /c, substantial bottom enrichment is possible, if backgrounds due to light quark production can be held to reasonably low levels. A fitting technique has been devised that yields the flavor composition of lepton tagged hadronic events as a function of the lepton p and p_T cuts [26]. In what follows, we will outline this method and summarize the results

The lepton tagged hadronic data sample contains contributions from five classes of events:

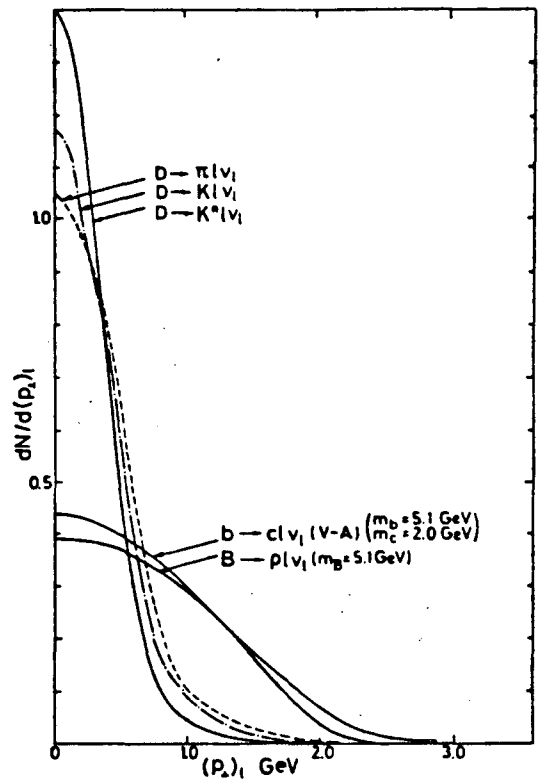

Figure 3.3: Transverse momenta spectra for leptons in heavy hadron semi-leptonic decays.

1. Prompt leptons from b-decay in $b\bar{b}$ events.
2. Prompt leptons from c-decay in $b\bar{b}$ events.
3. Prompt leptons from c-decay in $c\bar{c}$ events.
4. Background from non-prompt leptons.
5. Background from misidentified hadrons.

It should be noted that the background does contain a component of heavy quark events.

In the previous section, the contributions to the background are given as functions of lepton candidate p and p_T. One can therefore subtract the background from the data bin by bin to obtain the prompt lepton contributions within each p,p_T range.

To separate the three categories of prompt lepton signal (1-3 above), one must

appeal to a Monte Carlo model of the relevant quark hadronization and weak decay processes. Firstly, as has already been mentioned in the Monte Carlo description, the generated rest frame momentum spectra of prompt leptons for both bottom and charm decay are adjusted to agree well with observation. Secondly, the Monte Carlo incorporates the known hard heavy quark fragmentation using the Peterson *et.al.* parameterization described in Chapter 1. Finally, the Monte Carlo is used to determine the probability that a semi-leptonic decay of a heavy hadron with fragmentation energy fraction z produces a lepton within a given p,p_T bin. These binned Monte Carlo probabilities are used in a maximum likelihood fit designed to determine the composition of the prompt lepton signal. The analysis of reference 26 fixes $< z >_c$ at ≈ 0.55 in accord with measurements based on leptonic inclusive spectra and D^* fragmentation and a three parameter fit is performed to $< z >_b$, and the bottom and charm semi-leptonic branching ratios. The predictions of the fit for the total prompt lepton signal in each p, p_T bin were found to be in excellent agreement with the data. The reader is refered to reference 26 for futher details of the inclusive lepton analysis; figures 3.4 and 3.5 graphically summarize the results. The data shown in the figures above represent a small fraction of the total dataset. These results for the flavor enrichment as a function of the lepton tagging cuts are confirmed by recent studies that use the full 207pb^{-1} of data [29].

For the purposes of this thesis our main concern will be with the flavor composition of heavy quark enriched lepton tagged data. The inclusive lepton analysis can be used to determine the composition factors within arbitrary lepton p and p_T constraints. We will be using the bottom and charm enriched regions defined by

$$\mathrm{b-region} \ : \ \mathrm{p} > 2 \ \mathrm{GeV}/\mathrm{c} \ , \ \mathrm{p_T} > 1 \ \mathrm{GeV}/\mathrm{c}$$

$$\mathrm{c-region} \ : \ \mathrm{p} > 2 \ \mathrm{GeV}/\mathrm{c} \ , \ \mathrm{p_T} < 1 \ \mathrm{GeV}/\mathrm{c}$$

where the kinematic cuts are applied to the lepton candidate. The composition factors for these cuts are,

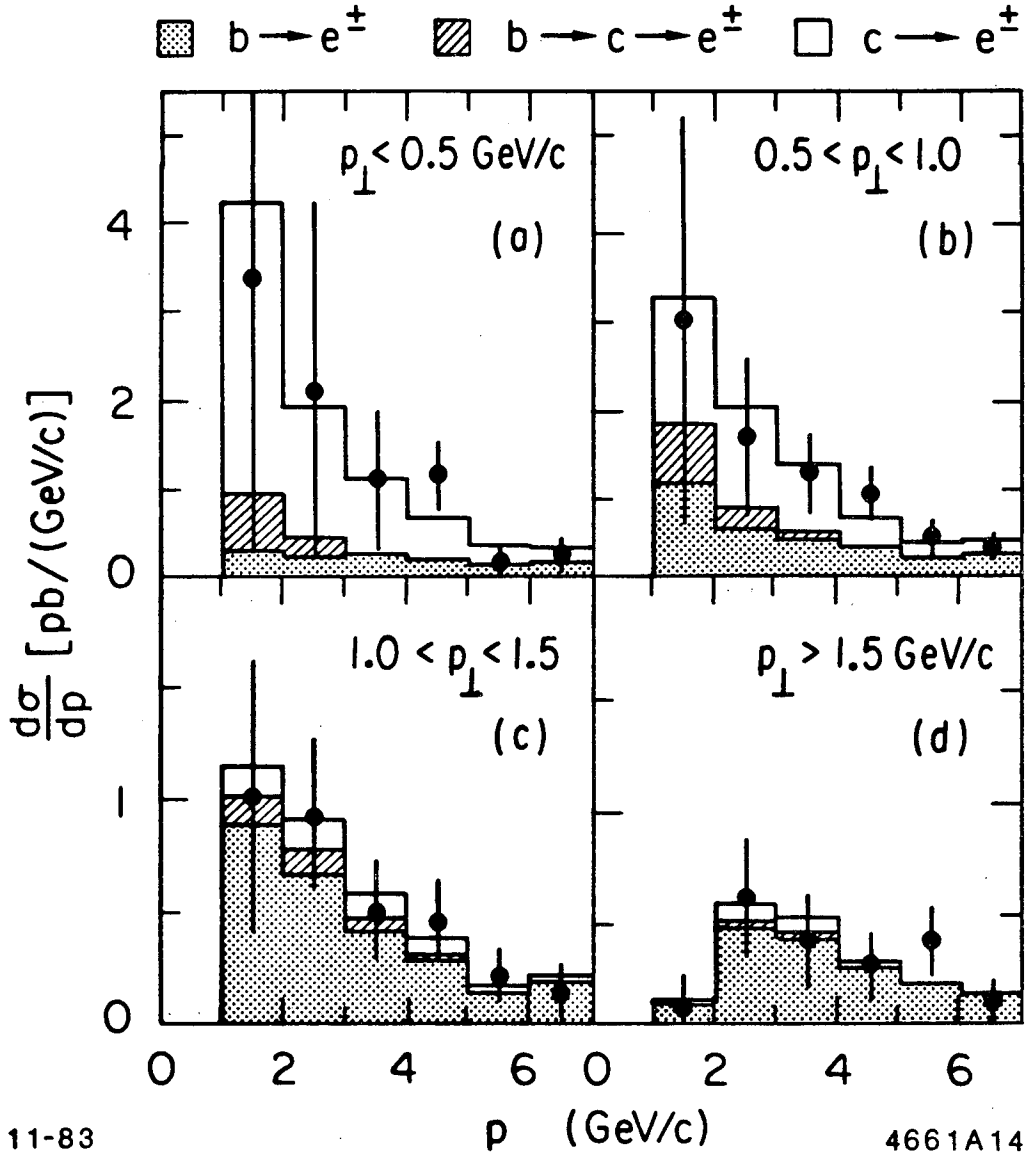

Figure 3.4: Fit composition as a function of electron cuts. The background subtracted electron momentum spectra for four regions of electron p_T are plotted (data points) along with the fit result (histogram). The composition of the fit within each momentum bin due to primary and secondary bottom and primary charm semi-electronic decay are indicated.

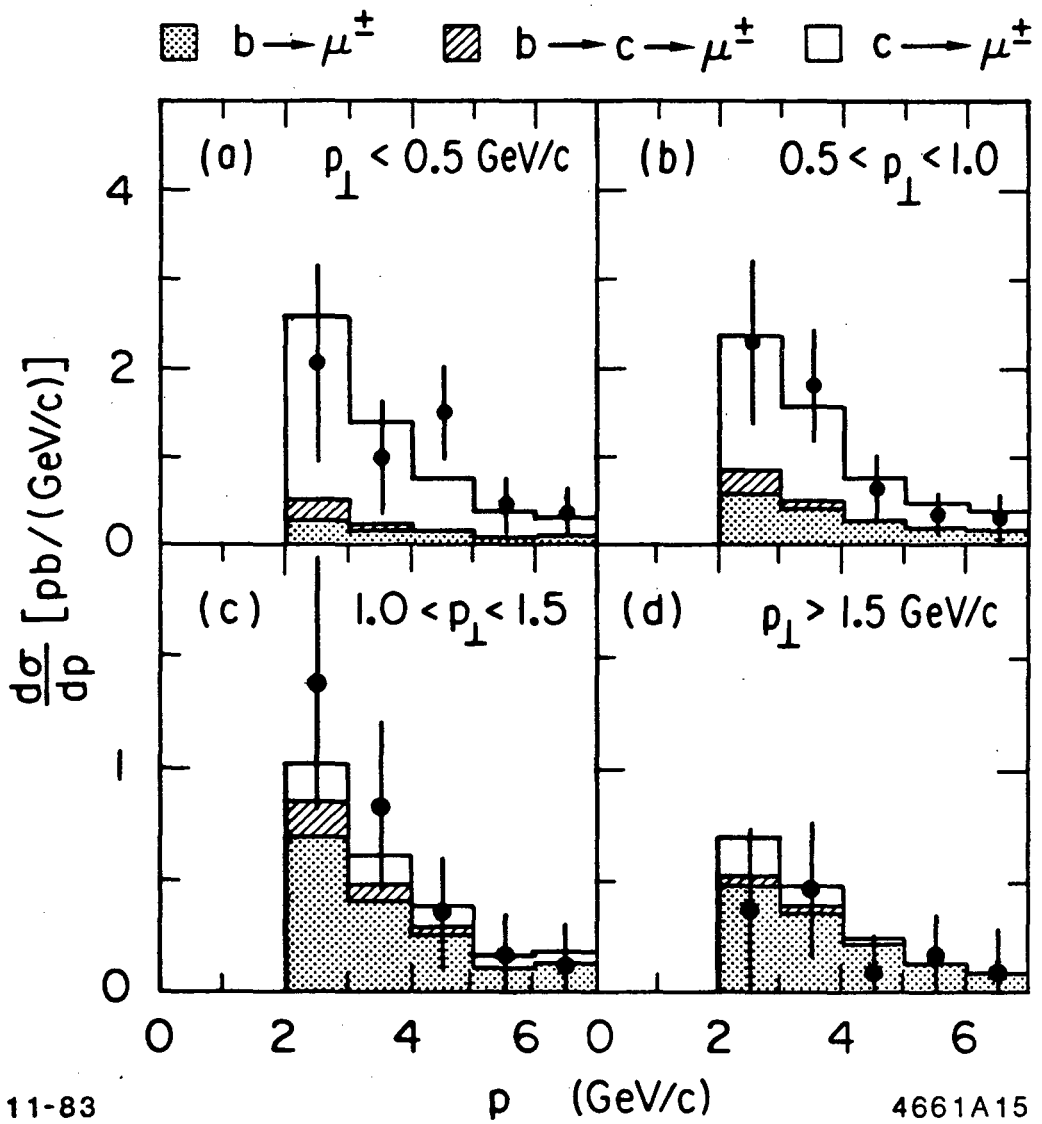

Figure 3.5: The same plot as Figure 3.4 using muons.

Region	$b\bar{b}$	$c\bar{c}$	*Background*
b-region	$64 \pm 8\%$	$16 \pm 8\%$	$20 \pm 8\%$
c-region	$19 \pm 8\%$	$35 \pm 8\%$	$46 \pm 8\%$

Table 3.5 : Flavor composition factors.

where the errors reflect both statistical and systematic uncertainties. The reader is reminded that the background consists of events where an incorrect prompt lepton identification is made, and does *not* represent an event sample due to primary light quarks alone. The $c\bar{c}$ component of the c-region can be increased to $\approx 45\%$ by changing the momentum cut to $p > 3$ GeV $/c$, at a cost of 48% of the statistics. Since the higher momentum cut was found to introduce unwanted bias in the study of c-event properties, the high statistics sample with the 2 GeV$/c$ cut was retained. This issue is discussed in more detail in Chapter 5.

3.7 Drift Chamber Performance

During the 1983 run the Mark II main drift chamber began to draw unacceptably high currents, and the chamber operating high voltages were lowered by $\approx 500\ V$ from their nominal $3000 - 3500\ V$ levels. These high currents, known as glow, were probably caused by the deposition onto the field wires of polymers formed from the ethane in the drift chamber gas. Since these polymers are insulating, they can lead to high electric fields at the wire due to the buildup of positive ions on the surface of the deposits. Due to the presence of high fields at the wire surface, field emission of electrons occurs with a resulting electron drift towards the sense wires that can lead to the rapidly rising current characteristic of glow. The lowering of field wire voltages prevents this runaway current from developing, but has the unfortunate consequence of degrading the drift chamber tracking efficiency. The inefficiency is manifest for tracks that pass close to some of the sense wires. For the near tracks the arrival times of discreet clusters of electrons are widely spaced and for low gains (due to low voltages), the charge amplification at the wire for a single cluster may generate signals below the preamplifier threshold. For tracks sufficiently far from the wire, several clusters usually arrive nearly simultaneously,

and the instantaneous charge at the wire is large enough to trigger the electronics. The large fluctuations in timing information for the near hits leads to software track reconstruction inefficiencies.

The drift chamber glow problems were remedied by the addition of 0.7% oxygen to the nominal 50/50 argon/ethane gas mixture. Oxygen is highly electronegative, and effectively damps the electron drift currents that lead to glow. With the new gas mixture, voltages were raised back up by several hundred volts and a dramatic improvement in drift chamber performance was observed. Figure 3.6 shows the occupancy as a function of drift distance for a single drift chamber layer, before and after the addition of oxygen [30]. The reduced efficiency for small distances can be seen in the older data, but has disappeared following the oxygen fix. It is also clear that the long distance performance has not been degraded by the presence of oxygen, as evidenced by the unchanging large distance drop off at 15 – 20mm.

The preceeding description of the cause of our uneven drift chamber performance implies that the effect is due to a single track inefficiency, with little or no dependence on track momentum or event topology. We have verified this expectation by a comparison between pre-glow data and the 1983 dataset. We find no difference between the two sets of data when comparing the *shape* (but not the normalization) of plots of track multiplicity as a function of momentum, or mean event multiplicity as a function of event thrust.

For the purposes of correcting data for variable drift chamber efficiency, the data have been divided into six blocks as shown in Table 3.6.

Block	pb^{-1}	Remarks
VCSUM	19.2	Good quality, pre-glow
POOR	15.5	DC at reduced voltage
SPRING	11.4	same
SPRING2	57.9	DC inner layers voltage raised slightly
OXYGEN	24.2	Oxygen added, all voltages close to nominal
NEWDAT	79.8	Voltages normal, oxygen in gas

Table 3.6 : Data Blocks.

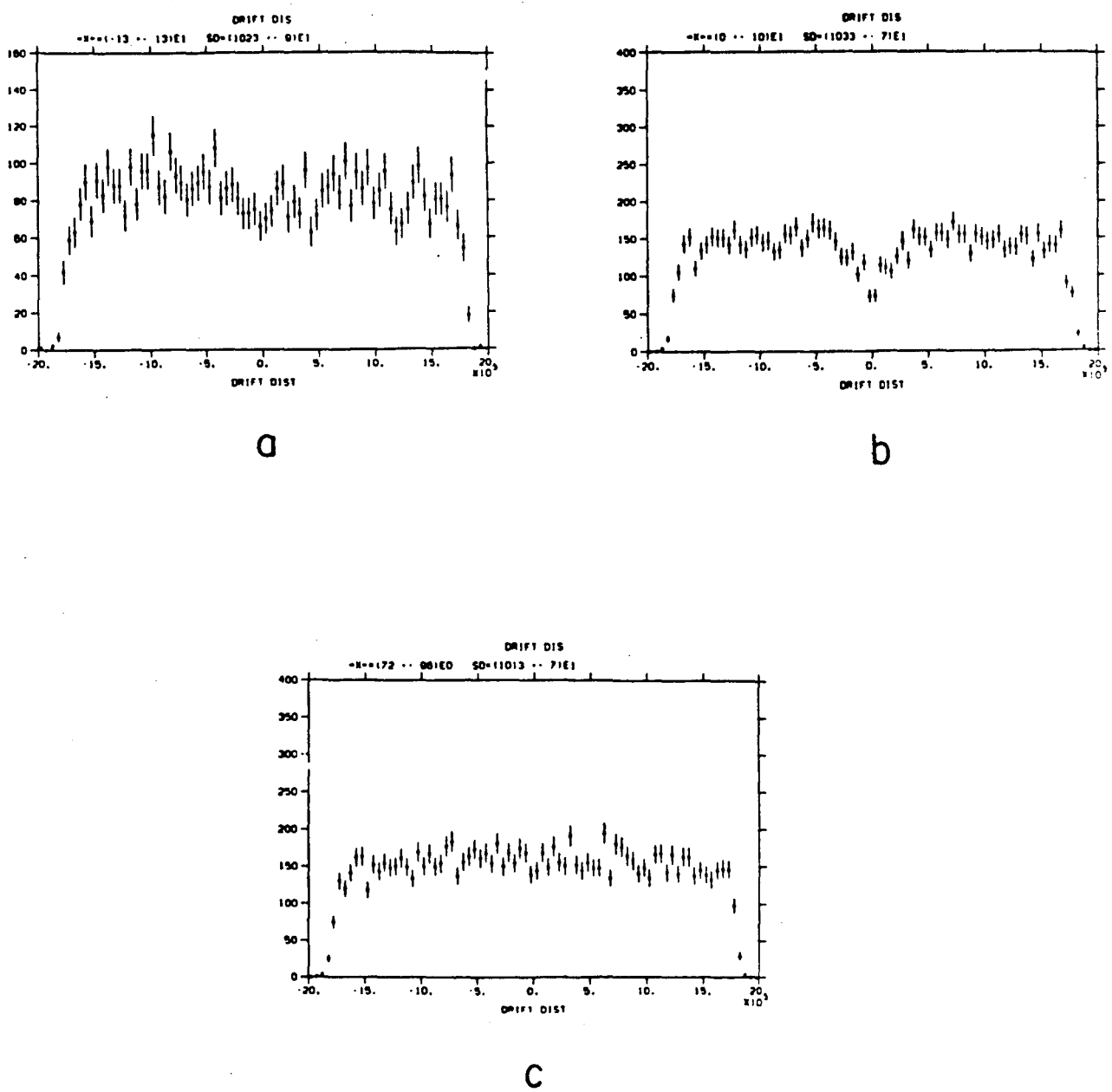

Figure 3.6: DC layer 12 occupancy as a function of drift distance before efficiency problems (a), during low voltage running (b) and after the addition of Oxygen to the DC gas mixture (c).

In Chapter 5 we will describe a data quality correction procedure.

4. Properties of Heavy Quark Jets

Once the flavor enriching lepton tag has been understood and quantified, the properties of bottom and charm jets can be studied in a relatively bias free way by examining the side of the event *opposite* to the tagging jet. This is accomplished by dividing the events in two (tag side and opposite side) with a plane perpendicular to the event thrust axis. This technique relies on the separated two jet topology of typical hadronic events at 29 GeV. By examining various inclusive properties of the opposite jet, one studies differences between heavy quark enriched jets and typical hadronic jets. Published results from other e^+e^- collaborations have noted little difference between charm jets and jets in typical events, but they report that bottom jets appear to be distinguishable [31, 32]. This analysis arrives at similar conclusions.

In this chapter we will describe measurements of the momentum, transverse momentum, rapidity and jet mass distributions of bottom and charm enriched events. The charged particle multiplicity of these events proved to be a particularly interesting property, and the next chapter is devoted to a much more detailed study of this measurement alone. The predictions of our Monte Carlo, which incorporates all that is reliably known about B and D meson decays and heavy quark fragmentation, will be compared with each of our observations. The relevant details of the Monte Carlo have been discussed in Chapter 3.

The b and c-region datasets will be simulated with $b\bar{b}$ and $c\bar{c}$ Monte Carlo data added in the appropriate proportions to sets of weighted simulated background made with real data. The background simulation method is described in the next section.

4.1 The Simulation of Backgrounds

The background to the prompt lepton signal has been discussed in Chapter 3. The background to the heavy quark prompt lepton signal in both the b and c-regions falls into two categories: events with misidentified hadrons, and events with non-prompt leptons. We now address the question of how to employ what we know about the lepton background to understand the properties of the background events. Straightforward application of our Monte Carlo is unsatisfactory, mainly due to the inadequate simulation of showering hadrons in the LA calorimeter. We will describe a background simulation method that is designed to be as Monte Carlo independent as possible, and will defer discussion of issues that require a full Monte Carlo analysis until the next chapter.

We have at our disposal detailed information regarding the accuracy of our lepton identification algorithm in the form of the probability tables given in Chapter 3 . In principle, one could use these probabilities to sample from a large hadronic dataset and thereby obtain a collection of events that would model the background. Instead, we use the following event weighting procedure. Recall that the misidentification probabilities in Tables 3.2 and 3.4 are binned by lepton candidate p and p_T, and that these tables combine all contributing processes: the muon table includes the effect of hadron punch through and non-prompt muons due to pion and kaon decays, while the electron table includes the effect of showering hadrons and overlap. The strategy is to assign a weight to an event that is a measure of the probability that that event could be included in the background, where the event weight is calculated from individual track misidentification probabilities. For a track to receive a non-zero weight, it must satisfy several criteria:

1. The track must satisfy the standard quality criteria.
2. The track must pass the relevant (b or c-region) p and p_T cuts.
3. The track must *not* be an identified lepton.

Next, we separately determine the fake muon and fake electron track weights. For a non-zero fake muon weight, the track must be within the muon fiducial volume The track is then assigned a fake muon weight appropriate to the track p and p_T.

Since all quality tracks are within the electron fiducial volume, the electron fakeness weight is assigned according to track p and p_T, with one possible exception. If the track in question is identified as a member of an e^+e^- conversion or Dalitz pair, the assigned weight is set equal to the pairfinder's *inefficiency* in the relevant p, p_T bin (Table 3.3). This special case occurs only a few percent of the time, but typical misidentification probabilities are $O(10^{-2})$ whereas the pairfinder inefficiencies are about 30%.

A typical event has an associated set of track weights $\{e_i\}$ and $\{\mu_i\}$, where a given track may have both an electron and a muon fakeness weight. For a single track, the probability that it could be a fake lepton is:

$$l_i = e_i + \mu_i - e_i\mu_i$$

The probability that the event contains at least one fake is given by:

$$\text{Event Weight} \equiv W = 1 - \prod_{i}^{tracks} (1 - l_i)$$

About 29% of the hadronic event sample has a finite b-region weight, to be compared to 75% for a finite c-region weight. For the b-region background events with *finite* weight, there are typically 1.23 potential lepton fakes per event with a mean event weight of 0.020. The corresponding numbers for the c-region background are 1.87 and 0.032. Additional details concerning the background simulation are given in the next chapter.

Simulated background events for both the b and c-regions are combined with Monte Carlo pure flavor ($b\bar{b}$ and $c\bar{c}$) events that contain prompt leptons. The Monte Carlo events are subjected to an analysis procedure identical to the one used for data. The composition of the simulated b and c-regions in terms of absolute weights is given below.

Simulated Enriched Regions			
Region	$b\bar{b}$	$c\bar{c}$	Background
b-region	176	44	55.0
c-region	174	320	420.6

Table 4.0

The relative composition of these samples is designed to be identical to the deduced flavor enrichment in the data. The statistics in the simulated b-region are limited by the number of $c\bar{c}$ Monte Carlo events that contain a high p_T lepton.

A relatively rare class of backgrounds is not accounted for by the simulation procedure. These events have a distinctive signature in the Mark II detector; an isolated high momentum electron recoiling against a hadronic jet. Occasionally a second opposite sign electron is detected, usually at a small angle to the beamline (Figure 4.0 shows a cross sectional view of two such events in the Mark II).

These events are largely due to higher order QED processes such as two photon processes or radiative Bhabha scattering where an initial or final state electron radiates a high energy photon which subsequently materializes as hadrons (see Figure 1.1). In the original inclusive lepton analysis, using a sample of 35pb^{-1}, about a dozen of these events were removed by handscan. For the full data sample, a set of cuts have been devised to eliminate these events [33]. Events are removed if:

1. $p^{electron} > 10$ GeV
2. or $p_T^{electron} > 2.5$ GeV
3. or electron $E_{LA} > 10$ GeV
4. or the electron is isolated in the x,y plane by more than 90^0 from the nearest charged track.

These cuts reduce the b-region from 688 to 645 events, and the c-region from 2094 to 2079 events. The effect of this small subtraction is non-neglible for the measurements of momentum spectra.

For the remainder of this chapter we will confine the data analysis to the high quality data blocks: VCSUM,OXYGEN, and NEWDATA, corresponding to a total

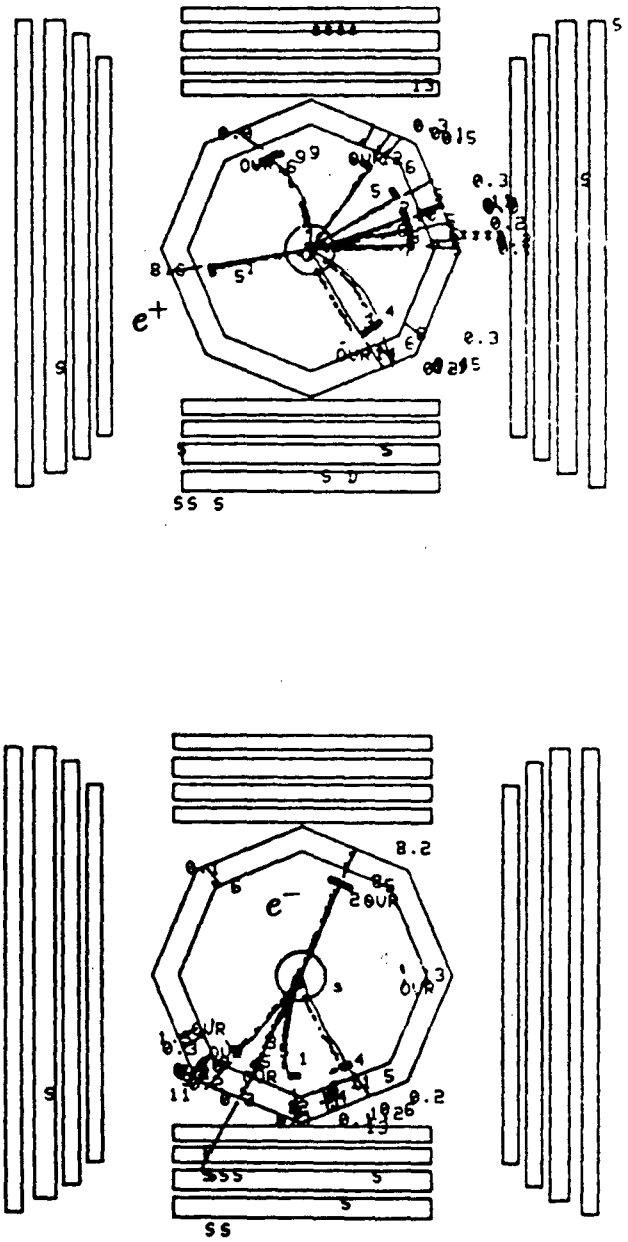

Figure 4.0: High order QED background events in the Mark II detector. The isolated electron track candidates are labeled.

integrated luminosity of 123 pb^{-1}. For the high quality data, the b and c-enriched regions consist of 391 and 1312 events respectively. In Chapter 5, the multiplicity analysis will include the full data sample by means of a data quality correction method.

4.2 Momentum Distributions

From the set of selected tracks for each event, the distributions in the jet opposite to the lepton tag for both momentum and p_T^2 with respect to the jet axis (determined from the tracks in the opposite jet) are shown in Figures 4.1 and 4.2 below.

The lower mean momentum for the b-region reflects the high particle multiplicity of these events: 1.27 ± 0.03 GeV$/c$ for the b-region and 1.46 ± 0.02 GeV$/c$ for the c-region. The Monte Carlo yields means of 1.20 ± 0.03 GeV$/c$ and 1.34 ± 0.03 GeV$/c$ respectively. The agreement between data and Monte Carlo is good for the b-region, but less satisfactory for the c-region due to a broader tail in the data than in the Monte Carlo distribution. Average p_T^2 of the bottom enriched data is 273 ± 13 MeV$^2/c^2$ compared to the c-region mean of 238 ± 7 MeV$^2/c^2$; the Monte Carlo results are 233 ± 12 MeV$^2/c^2$ and 217 ± 8 MeV$^2/c^2$. Even if one allows for the fact that our data regions are only partially enriched, these differences between the two heavy flavors are not dramatic enough to be useful for flavor tagging. As can be seen in the figures, the agreement between the Monte Carlo and the data is good, allowing one to assume that heavy quark fragmentation and decay as implemented in the Monte Carlo is satisfactory.

4.3 Rapidity Distributions

The distributions in the opposite jet for rapidity, defined as:

$$\eta = \frac{1}{2}\ln\left(\frac{E + p_{\|}}{E - p_{\|}}\right)$$

where the defining axis is the jet thrust axis and pion masses are assigned to all tracks, are shown in Figure 4.3 . The DELCO collaboration has previously reported

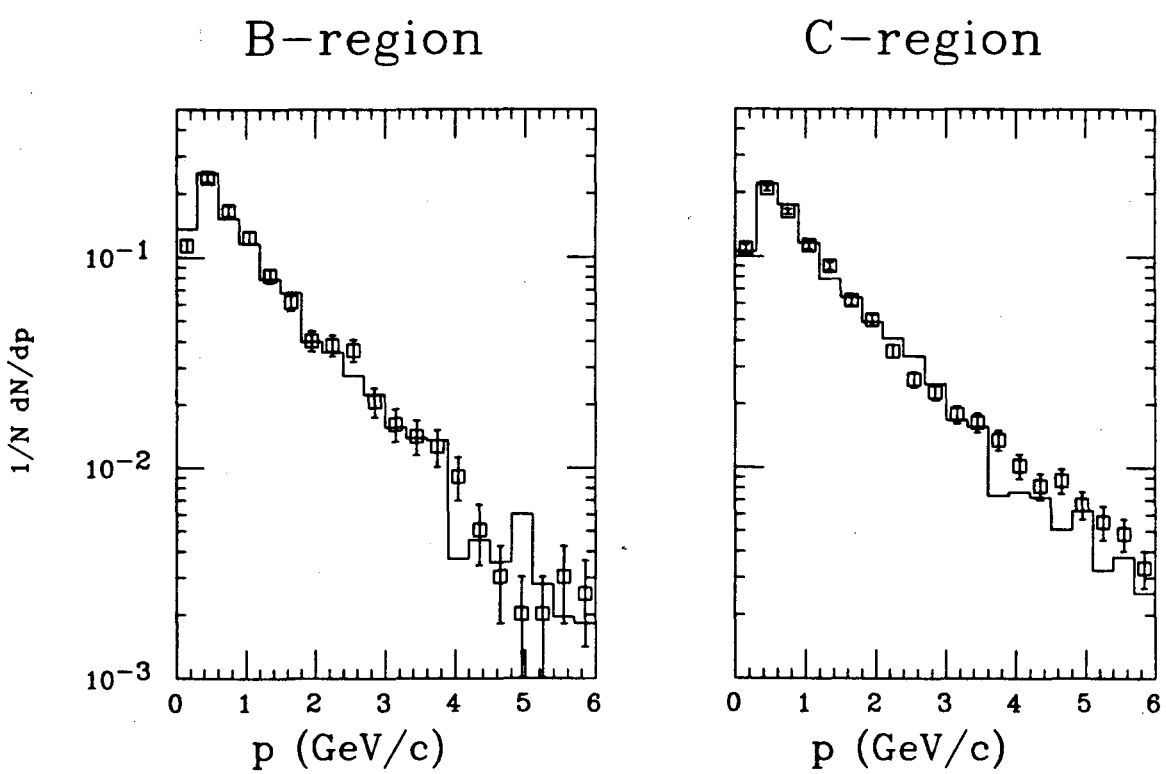

Figure 4.1: Inclusive momentum distributions opposite a tag lepton for the b- and c-regions. The solid line is the result for simulated data.

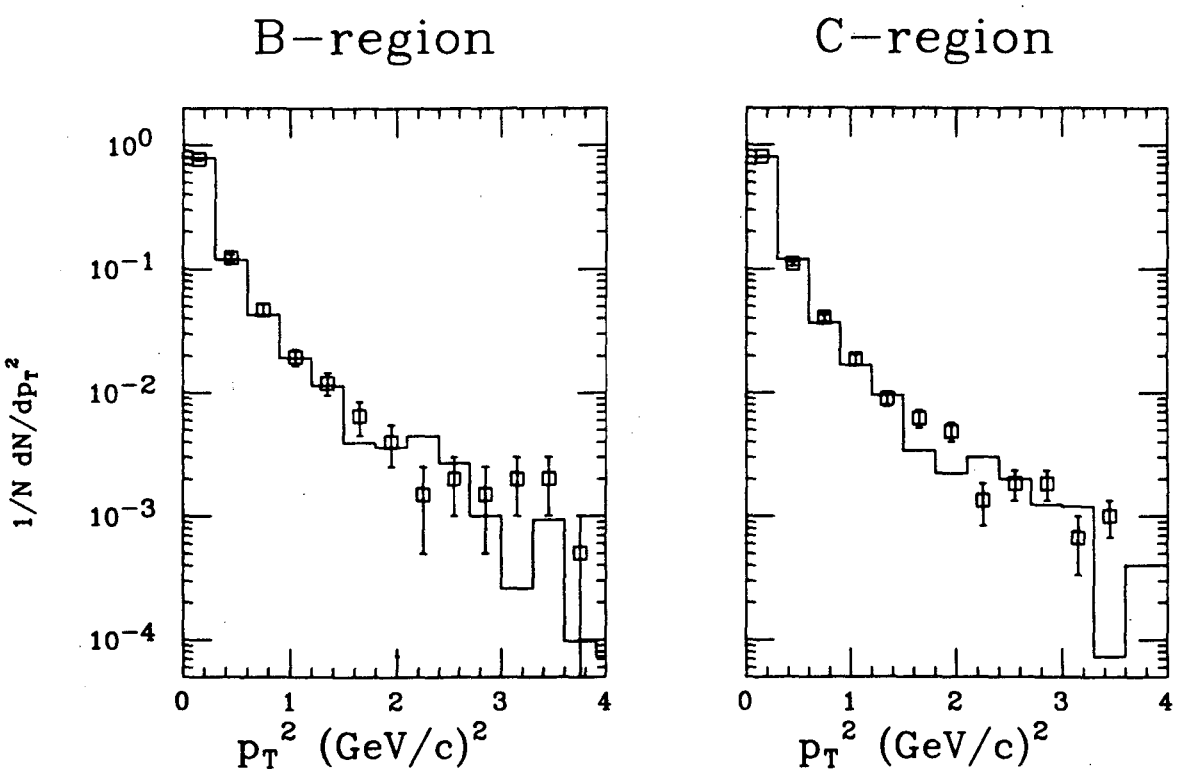

Figure 4.2: Inclusive p_T^2 distributions opposite a tag lepton for the b- and c-regions. The solid line is the result for simulated data.

a difference in the shape of the rapidity distributions of b-jets relative to average or c-jets [32]. We observe a similar narrowing of the rapidity plot for b-jets, in agreement with the DELCO results. As expected, the effect seen in this analysis is less pronounced than that reported by DELCO due to the substantially higher b-enrichment ($83 \pm 6\%$) of the DELCO data when compared with the Mark II b-region ($64 \pm 8\%$).

The enhancement in b-jets at $\eta \approx 1 - 2$ and the depopulation of the higher rapidity region ($\eta > 3$) is due to the contribution of the high multiplicity and large average p_T of bottom hadron decay products. As a check, the Monte Carlo is used to separate out the component of the rapidity plot due to b-decay products, and it is found that these particles preferentially populate the mid-range rapidities when compared to the non-leading contributions. The mean rapidities for the b and c-region data (Monte Carlo) are 1.44 ± 0.02 (1.39 ± 0.02) and 1.58 ± 0.01 (1.53 ± 0.02).

4.4 Jet Invariant Mass

To some extent, the large masses of charm and bottom quarks should be reflected in the invariant mass of the produced hadronic jet. The contribution of non-leading fragmentation products will obscure this effect; the mass of a hadronic jet is not expected to equal the mass of the primary quark. Nevertheless, the mass of a bottom jet should exceed the mass of a typical jet or charm jet. Due to the finite angular acceptance of the Mark II, and to the potentially large component of missing neutral energy in hadronic events, the straightforward calculation of jet mass using reconstructed 4-vectors will yield a consistently low result. A better estimate of the mean jet mass can be obtained from the topology of the jet as characterized by the jet thrust, a normalized quantity that is meaningful even for an incomplete set of 4-vectors. The jet mass, given by

$$M_{jet} = (E_{jet}^2 - P_{jet}^2)^{1/2}$$

can be approximately related to the jet thrust, given by

$$\mathrm{T} = \mathrm{max}_{\mathbf{T}}\left(\frac{\Sigma|\mathrm{p}_{\|}|}{\Sigma|\mathrm{p}|}\right)$$

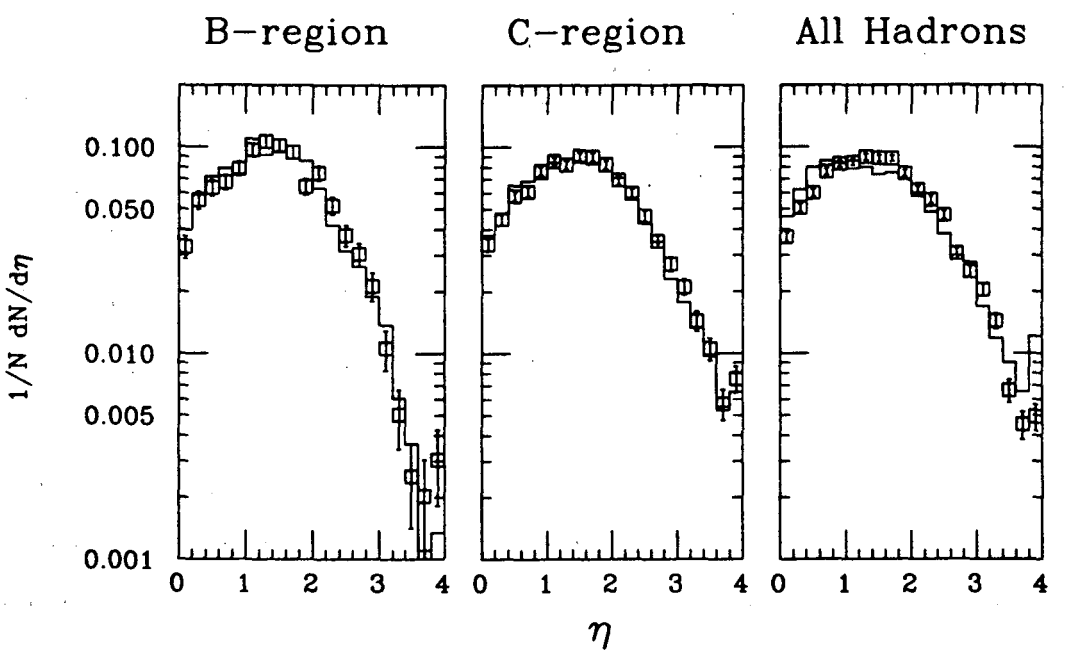

Figure 4.3: Inclusive rapidity distributions opposite a tag lepton for the b and c-regions and for average hadron jets. The solid line is the result for simulated data.

(where the T axis is the axis that maximizes thrust). Assuming that the thrust axis is a good measure of the true jet direction, and that the total p_T within a jet balances to zero, we have

$$M_{jet} = E_{jet}(1 - \frac{(\Sigma|p_{\|}|)^2}{E_{jet}^2})^{1/2}$$

Neglecting particle masses ($|p| = E$) while taking E_{jet} equal to the beam energy (14.5 GeV) we finally obtain

$$M_{jet} = E_{beam}(1 - \mathrm{T}_{jet}^2)^{1/2}.$$

The mass distributions for the b and c-regions, calculated using both 4-momenta and thrust are shown below (Figure 4.4). The results for an average hadronic sample are also shown (where the opposite jet, in the absence of a tag lepton, is chosen at random with respect to the thrust plane).

There is good agreement between the data and Monte Carlo samples in all cases. The mean thrust jet mass for the charm-enriched data (Monte Carlo) is significantly lower, 5.1 ± 0.05 GeV $/c^2$ (5.4 ± 0.07 GeV $/c^2$), than that for the bottom sample, 6.2 ± 0.1 GeV$/c^2$ (6.3 ± 0.1 GeV$/c^2$), an effect also evident for the 4-vector jet masses of 3.9 ± 0.05 GeV$/c^2$ (3.5 ± 0.05 GeV$/c^2$) and 4.3 ± 0.1 GeV$/c^2$ (4.0 ± 0.1 GeV$/c^2$) . The c-region distribution is consistent with a jet mass plot made for an average hadronic data (Monte Carlo) sample, where the mean thrust and 4-vector jet masses are 5.6 ± 0.05 GeV$/c^2$ (5.7 ± 0.05 GeV$/c^2$) and 3.9 ± 0.05 GeV$/c^2$ (3.7 ± 0.04 GeV$/c^2$) respectively.

The two main conclusions of this chapter are: (1) for the distributions discussed, b-jets show clear differences when compared to c-jets or average jets, and (2), these differences are well represented by our Monte Carlo. The sizable differences in event topology between bottom and charm have prompted some groups, for example the TASSO and JADE collaborations At DESY, to devise methods that use event shape parameters to achieve flavor enrichment [34, 35]. We will instead point out the importance, to future experiments at higher energy e^+e^- colliders (LEP at CERN or

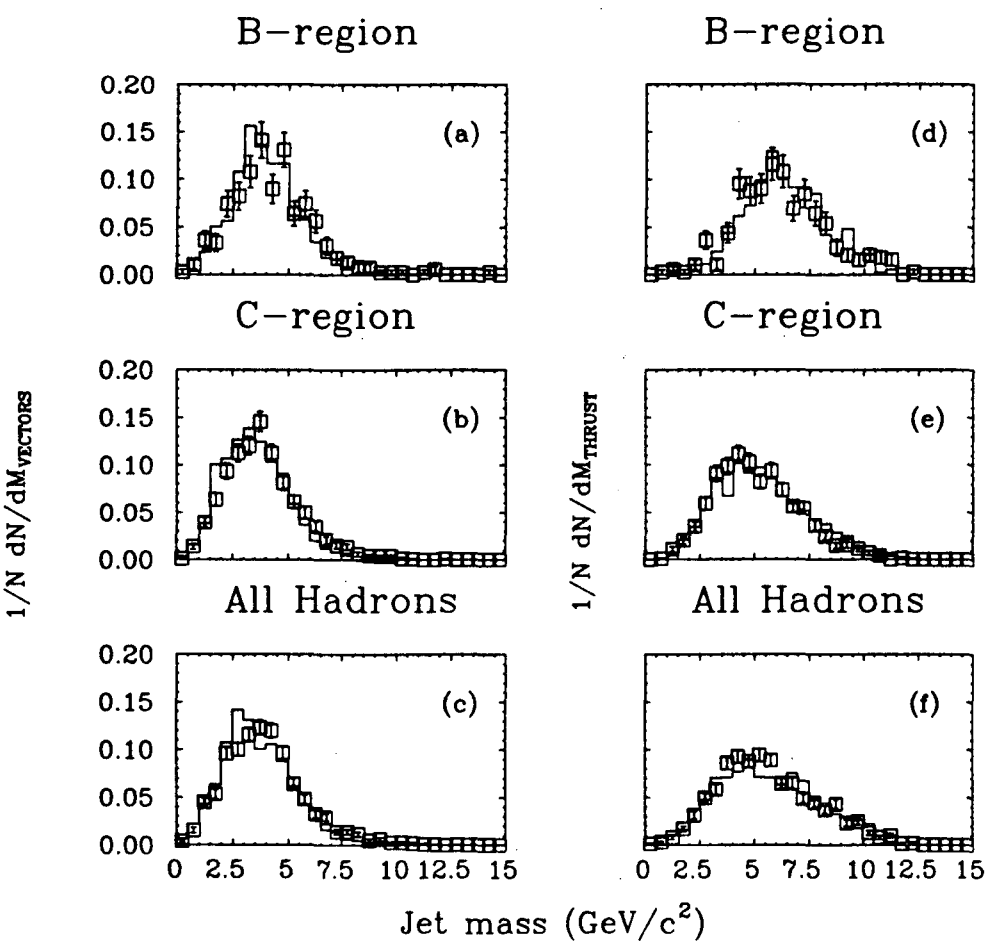

Figure 4.4: Opposite jet mass distributions calculated both with 4-vectors (a-c) and thrust (d-f) for both the b and c-regions, and for average hadron jets. The solid line is the result for simulated data.

the SLC at SLAC), of a Monte Carlo that properly simulates heavy quark hadronic events.

5. Properties of Heavy Quarks Events: Charged Particle Multiplicity

The relatively large rest masses of charm and bottom states suggests that the decay multiplicity of heavy quark hadrons should be high relative to the light quark states. This expectation is in fact born out by measurement. Typical D meson decay charged multiplicities are 2.5 [14], while for the heavier B-meson, the number is 5.5 [25]. From these heavy meson mean decay multiplicities, one might naively expect to see a large difference in the charged multiplicity of heavy quark jets relative to light quark jets, or charm jets compared to bottom jets. The situation is, however, complicated by the fact that in e^+e^- annihilation at high energies (away from the the vector meson resonances), a significant proportion of particle production is due to strong and electromagnetic interactions that precede weak decay processes. In the case of heavy flavor production, it is experimentally convenient to distinguish *leading* particles, i.e. those particles deriving directly from the decay of the heavy flavor hadrons, from $non-leading$ particles deriving from all other sources. This classification is possible due to the very strong suppression of heavy quark pair production from the vacuum ; heavy hadrons contain the primary heavy quarks. The non-leading multiplicity is related to the details of quark fragmentation, as we describe in what follows.

It is now well established that heavy quarks produced in e^+e^- annihilation carry a large fraction of the available beam energy [20]. We define this fraction to be $z = \frac{E_h}{E_q}$ where E_h is the generated heavy hadron energy and E_q is the primary heavy quark energy. Analyses of inclusive lepton [27, 36, 37, 38, 39], and D^* spectra [31, 40, 41, 42] have indicated that mean z is typically ≈ 0.6 for charm quarks, and ≈ 0.8 for bottom quarks. Hard quark fragmentation bears directly on the magnitude of non-leading multiplicity due to the dependence of multiplicity on available energy.

In particular, non-leading multiplicity in $c\bar{c}$ and especially in $b\bar{b}$ events is expected to be smaller than it is for light quarks. Even though the charged multiplicity of bottom hadron decay is significantly larger than it is for charm hadrons, these large differences in multiplicity due to weak decays may be effectively compensated by differences in non-leading multiplicity in hadronic jets.

We will describe a multiplicity measurement of charm and bottom enriched data. The non-leading and leading components of the charged multiplicity will be separated by using available heavy meson decay multiplicity data from SPEAR and CESR experiments. Our approach will proceed in several steps as follows:

1. Perform a multiplicity unfold of the observed multiplicity distibutions for the c and b enriched regions.
2. Estimate the background contribution in each region using available lepton misidentification data.
3. Extract the pure $c\bar{c}$ and $b\bar{b}$ mean event multiplicities using the known flavor composition factors for each enriched region.
4. Apply final corrections to the results. We will also need to account for non-uniform data quality due to variable drift chamber efficiency. This will be done at step 1 by an appropriate modification of the unfold procedure.

An average hadronic sample will also be analysed and compared with the results for the tagged data.

5.1 Multiplicity Unfold

An observed charged multiplicity distribution represents, insofar as backgrounds are accounted for, a degraded version of a parent distribution that arises due to the finite tracking efficiency of the detector. If the single track efficiency is ϵ, and all possible track to track correlations are negligible, the observed distribution is related to the produced distribution by:

$$N_q = \sum_{p \geq q}^{p_{max}} \frac{p!}{q!(p-q)!} \epsilon^q (1-\epsilon)^{p-q} \eta_p \tag{1}$$

where:

$$N_q \equiv \text{ observed distribution } \eta_p \equiv \text{ produced distribution.}$$

The q run over the observed and the p over the produced multiplicities, where η_p is non-zero only for p even. In the simplest case, where tracks are produced isotropically in an isotropic detector and tracking efficiency is momentum independent, ϵ is given by the fraction of instrumented solid angle. At SPEAR energies, due to the near-spherical topology and low multiplicity of charmonium decays and off resonance jet events, this crude approximation worked suprisingly well [43]. At PEP, where collimated jets and high multiplicities result in a crowded tracking environment, the situation is more complicated. One must therefore generate a general unfold efficiency matrix by Monte Carlo. The unfold efficiency matrix is defined by:

$$\epsilon_{pq} = \frac{\text{number of times q tracks observed when p tracks produced}}{\text{number of times p tracks are produced}}$$

The produced track count is the total number of charged Monte Carlo tracks exclusive of those arising from pair conversions or Dalitz decays. Thus the two charged tracks from K_s and Λ decay are included.

The resulting matrix is nearly model independent, in the sense that the Monte Carlo detector simulation, rather than the event generation algorithm, largely determines the values of the matrix entries. Observed multiplicities at PEP range up to 20, implying substantially higher produced multiplicities. For an unfold matrix of this size, considerable Monte Carlo statistics are required before typical fluctuations among the matrix entries fall to acceptable levels. An average hadronic sample (no lepton tag) is used to generate our matrix since robust statistics are needed. Due to the low efficiency of the lepton identification criteria and of the lepton kinematic cuts, the b or c-enriched regions are too sparse to be used for matrix generation without the need for impractically large or inherently biased Monte Carlo statistics. However, the matrix generated from an overall hadronic sample was found to introduce a small bias when used to unfold the lepton tagged samples, due to the presence of at least one high momentum track in the tagged data that

may be absent in an ordinary hadronic event. The matrix finally used to unfold the b and c-enriched regions and their backgrounds was generated with the additional requirement that the event contain a selected track with momentum of ≥ 2 GeV. Roughly 25,000 events were used to fill the matrix. Tests using Monte Carlo data indicated an improvement in the accuracy of the unfold when the modified matrix was used (a matrix made without the high momentum track cut was used for the overall hadronic sample).

The unfold matrix contains all the information needed to make acceptance corrections to the observed multiplicity distributions. Due to the fact that the produced charged multiplicity must be an even number, a straightforward inversion of the matrix equation $N_q = \Sigma\epsilon_{pq}\eta_p$ is not possible; the equations are over-constrained. Instead, a maximum likelihood fit is used to determine the η_p. In general, each η_p would be separately varied in the fit, but we found this multiparameter fit to be numerically unstable due to fluctuations in the data, and to a lesser extent, in the unfold matrix. We have used a two parameter fitting function given by:

$$P_{\mu,a}(p) = N(\mu, a)\frac{e^{-\mu/a}(\mu/a)^{p/a}}{\Gamma(p/a+1)} \quad , p \text{ even.} \tag{2}$$

where both μ and a, are taken as free parameters. This distribution (2) is a generalization of the Poisson distribution with mean value approximately equal to μ and RMS width approximately equal to $\sqrt{\mu a}$. This form for the fitting function is motivated by the fact that charged particle production in hadronic events occurs in correlated groups, due to resonance and weak decays for example, and therefore should reflect a larger multiplicity variance than expected for a Poisson distribution. Hypothetically, if charge conservation constrains charged particle production to always occur in pairs, the multiplicity distribution for random pair production would be of the form of equation 2 with $a = 2$. The overall normalization factor $N(\mu, a)$ is absorbed by our normalization method that contrains the sum over all bins to be equal to the total number of observed events. The Poisson Likelihood fit proceeds as follows:

The expected number in bin q is,

$$\mu_q = \sum_{p=p_{min}}^{p_{max}} \epsilon_{pq} P_{\mu,a}(p) M(\mu, a) \tag{3}$$

and the normalization factor,

$$M(\mu, a) = \frac{\mathrm{N}}{\sum_q \sum_p \epsilon_{pq} P_{\mu,a}(p)}$$

insures that,

$$\text{total number of observed events} \equiv \mathrm{N} = \sum_q N_q = \sum_q \mu_q$$

The poisson likelihood function is :

$$\mathcal{L} = \prod_q \frac{\mu_q^{N_q} e^{-\mu_q}}{N_q!} \tag{4}$$

We maximize the log likelihood with respect to μ and a ,

$$\log \mathcal{L} = \sum_q N_q \log \mu_q(\mu, a) + constant \tag{5}$$

where the constant is independent of the fit parameters. The numerical package MINUIT, originally written at CERN, is used to find the minima in parameter space of the negative log likelihood [44]. With the two parameter function (2), an excellent fit can be achieved. Figure 5.0 shows a test fit to Monte Carlo hadronic event data; the observed multiplicity distribution, the parent distribution and the fit result.

5.2 Correcting for Non-uniform Data Quality

Recall that the data have been partitioned into blocks of approximately uniform D.C. efficiency (Table 3.6). In order to maximize the limited statistics of the b-enriched data, it is desirable to use as much of the collected luminosity as possible by correcting for the low efficiency data subsets. The average number of quality tracks found per average hadronic event is a measure of the track finding efficiency,

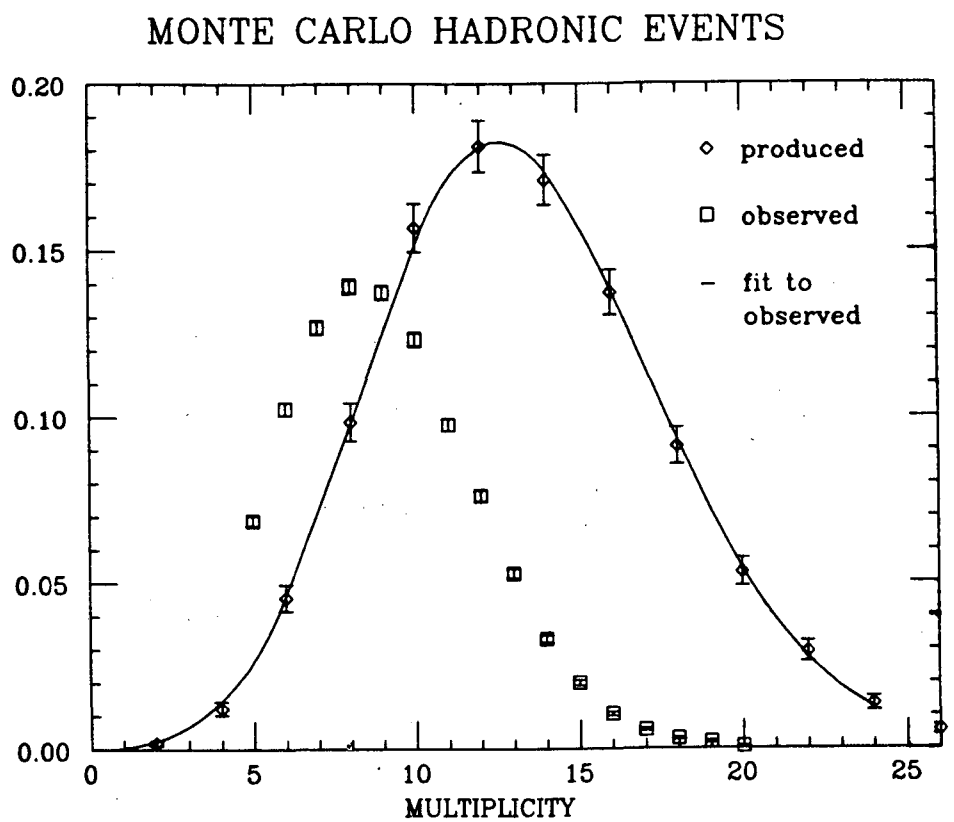

Figure 5.0: Results of a test fit to Monte Carlo hadronic events. The observed data, produced data and fit from the observed data are shown.

and VCSUM has, as a block, the highest efficiency. Using VCSUM as our standard, and having verified that the efficiency degradation in the lower quality blocks is a single track effect, we correct the four sub-standard blocks by the following procedure. (The NEWDAT block is treated on equal footing with VCSUM, and is not corrected).

Let ϵ be the efficiency correction factor for a given block ($\epsilon = 1$ for VCSUM). Then the corrected unfold matrix is given by :

$$\epsilon'_{pq} = \sum_{Q \geq q}^{p} \epsilon_{pQ} \frac{Q!}{q!(Q-q)!} \epsilon^{q} (1-\epsilon)^{Q-q} \tag{6}$$

The efficiency degraded multiplicity distribution may be obtained from the standard (in our case, VCSUM) distribution as shown :

$$N'_q = \sum_{Q \geq q}^{Q_{max}} \frac{Q!}{q!(Q-q)!} \epsilon^q (1-\epsilon)^{Q-q} N_Q \tag{7}$$

The correction factor ϵ is determined by hand . First, the VCSUM observed distribution is degraded according to eq. 7 for a test value of ϵ. Then ϵ is varied until the mean of the degraded distribution equals the mean of the distribution of the block in question. The fit between a given block's distribution and the appropriately degraded VCSUM distribution is good, as can be seen from Figure 5.1 (shown for the SPRING block).

Once all six matrices have been determined, separate block by block fits are performed, as well as a simultaneous fit to a generalized likelihood function,

$$\log \mathcal{L} = \sum_{blocks} \sum_{q} (N_q^i \log \mu_q^i) \tag{8}$$

where $i = 1, ...6$ and each block is individually normalized. The efficiency correction factors are found to be:

Block	ϵ
VCSUM	1.0
POOR	0.8960
SPRING	0.9075
SPRING2	0.9355
OXYGEN	0.9965
NEWDAT	1.0

Table 5.0 : Data block relative efficiencies

where the errors on these factors are approximately ± 0.005.

5.3 Background

The simulated background method has been outlined in Chapter 3. We now apply the multiplicity analysis to samples of background events. Having found a

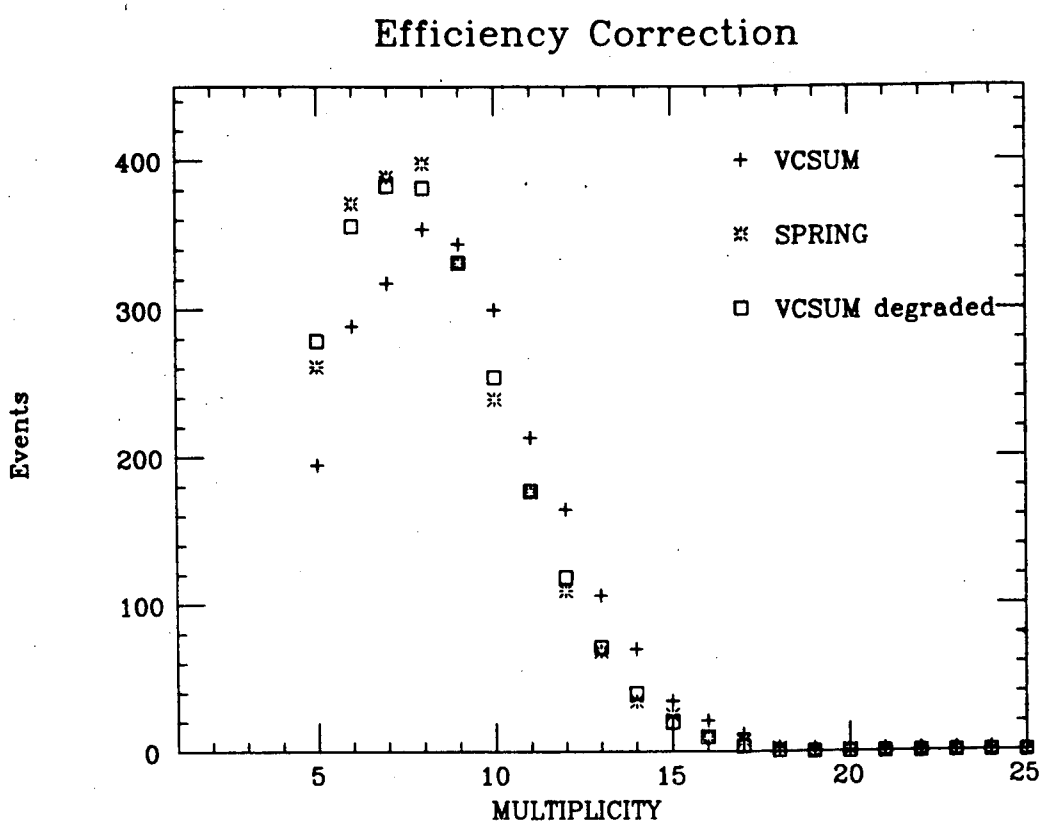

Figure 5.1: SPRING data block multiplicity distribution after efficiency correction. The high efficiency VCSUM data, before and after simulated degradation, are shown along with the SPRING distribution.

weight for an event, the analysis proceeds in the usual way (excepting lepton cuts), and weighted histograms are accumulated. In particular, weighted background multiplicity distributions are generated separately for each data block, and a fit is performed to extract the parent distributions.

The weighting procedure was originally designed to model approximately those effects that correlate multiplicity with the probability that a given event contains a fake lepton. For example, one might expect that the presence in the b-region of a high p_T lepton candidate would enrich the the background in this region with

bottom produced events, as well as with gluonic three-jet events, effects that tend to increase the mean event multiplicity. In order to better understand the produced properties of the background, Monte Carlo events were subjected to the weighting procedure given above.

Our Monte Carlo defines the arbitrary dividing line between two and three-jet events such that the minimum gluon energy in a three-jet event is 10% of the beam energy, or $\approx$ 1.5 GeV. Table 5.1 shows the percentage breakdown of gluonic events for various signal data subsets, while Table 5.2 gives the expected flavor composition of the two background groups. The errors shown are purely statistical. While the bottom enrichment in the b-region background is not very dramatic, a large enhancement of the gluonic component is evident (63%) when compared to its nominal ($\approx$ 25%) value. A similar gluonic enhancement occurs for $c\bar{c}$ events in the b-region. The Monte Carlo exhibits the higher non-leading multiplicity expected in three-jet events; the effect for both $b\bar{b}$ and $c\bar{c}$ events is shown in Table 5.1.

Monte Carlo Heavy quark events		
event type	% gluonic 3-jet	non-leading multiplicity
$b\bar{b}$ in b-region	$15 \pm 2\%$	5.7 ± 0.5
$b\bar{b}$ in c-region	$19 \pm 2\%$	5.6 ± 0.4
$c\bar{c}$ in b-region	$66 \pm 16\%$	9.0 ± 0.6
$c\bar{c}$ in c-region	$26 \pm 3\%$	7.6 ± 0.2

Table 5.1 : Properties of Monte Carlo signal events.

Monte Carlo Background events			
Region	% gluonic 3-jet	% $b\bar{b}$	% $c\bar{c}$
b-region	$63 \pm 0.6\%$	$19 \pm 0.2\%$	$29 \pm 0.3\%$
c-region	$28 \pm 0.02\%$	$7 \pm 0.04\%$	$37 \pm 0.2\%$

Table 5.2 : Properties of Monte Carlo background events.

5.4 Fit Results

Table 5.3 shows the fit results for parameters μ and a with their associated statistical errors, for five datasets: the full hadronic sample, the b-region, the c-region, and the two background regions.

Dataset	events	μ	a
Hadronic	46,112	12.7 ± 0.1	1.4 ± 0.1
b-region	645	13.9 ± 0.25	1.0 ± 0.2
c-region	2,079	12.6 ± 0.1	0.9 ± 0.1
b-region bkgrd	11,670	13.6 ± 0.1	1.2 ± 0.1
c-region bkgrd	30,180	12.6 ± 0.1	1.2 ± 0.1

Table 5.3 : Fit results.

Due to the fact that a subset of the hadronic events (the VCSUM block) is used to rescale the unfold matrices, the statistical error on the fit results for the full hadronic sample is conservatively taken to reflect the statistical weight of the VCSUM block alone ($\approx 9\%$ of the total sample). The b and c-regions are highly selected subsets of the full hadronic sample, and correlations between the data blocks within these samples can be ignored. The high multiplicity of the b-region background reflects the fact, mentioned above and also seen in our Monte Carlo, that the requirement of a high p_T track tends to enrich the background with high multiplicity three-jet events and with bottom events themselves.

Our concern will be mainly with the parameter μ which will be used to determine the mean multiplicities of $b\bar{b}$ and $c\bar{c}$ events. The fitted values of the width parameter a for the b and c-regions have sizable errors, and are subject to a bias that narrows the multiplicity distribution due to the presence of the high momentum tag lepton. The fit result for a for the full hadronic sample is sufficiently precise and bias free to be compared with existing measurements. We will postpone any discussion of the width parameter until the end of this chapter.

Figure 5.2 shows the observed multiplicity distributions for both the b and c regions, and the expected distributions deduced from our fits from the unfold matrices.

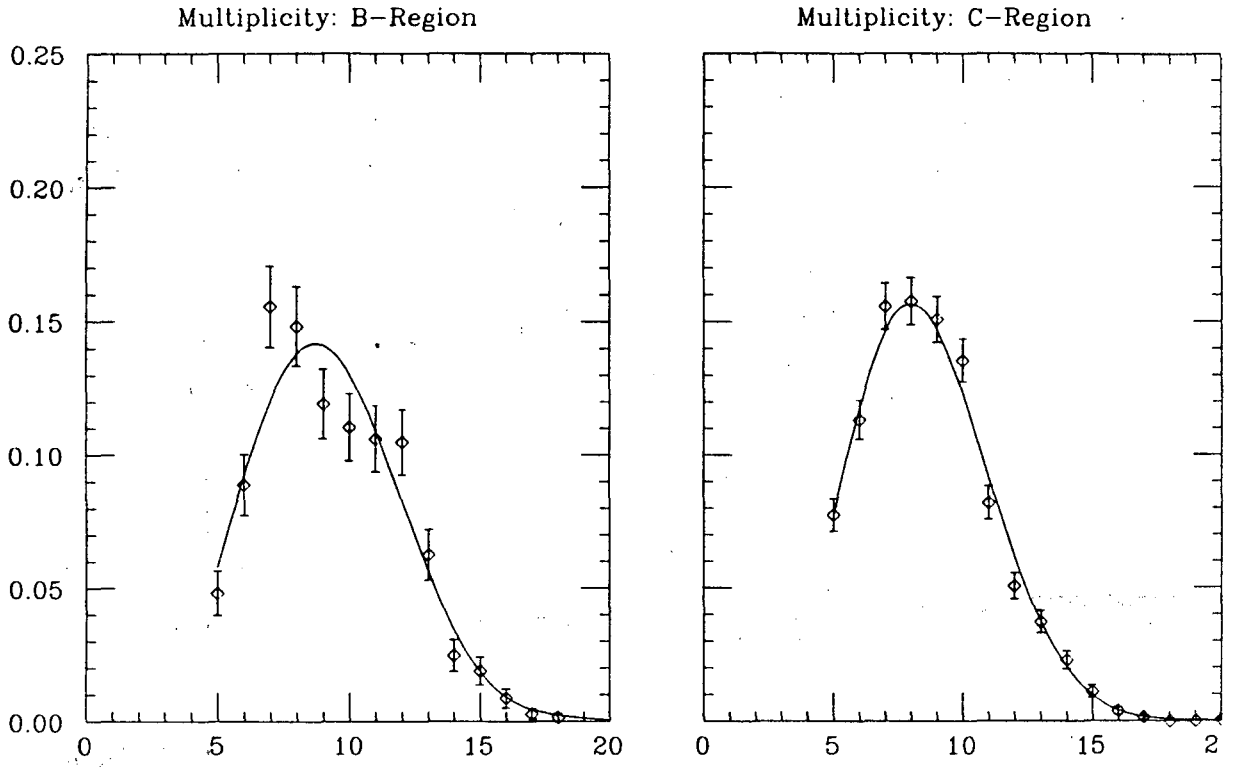

Figure 5.2: The b and c-region multiplicity distributions, and the result expected from the fit.

There is satisfactory agreement between the data and the expected distributions.

However, the fit is noticably better when restricted to only the high efficiency data (Figure 5.3).

We use the results for the tagged regions and their backgrounds to solve for the pure $b\bar{b}$ and $c\bar{c}$ event mean charged multiplicities from the equations,

$$\begin{aligned} \mu_b &= f_b^b m_{b\bar{b}} + f_c^b m_{c\bar{c}} + f_{bkgrnd}^b \mu_{bkgrnd}^b \\ \mu_c &= f_b^c m_{b\bar{b}} + f_c^c m_{c\bar{c}} + f_{bkgrnd}^c \mu_{bkgrnd}^c \end{aligned} \tag{9}$$

where the μ's are the four fit results, the f_x^X's are the x enrichment factors in the X-region and the m's are the unknown pure flavor mean multiplicities. The f flavor enrichment factors are restated here for completeness,

$$b-region: \quad 64\%\ b\bar{b},\ \ 16\%\ c\bar{c}\ \ and\ \ 20\%\ \ background$$

$$c-region: \quad 19\%\ b\bar{b},\ \ 35\%\ c\bar{c}\ \ and\ \ 46\%\ \ background$$

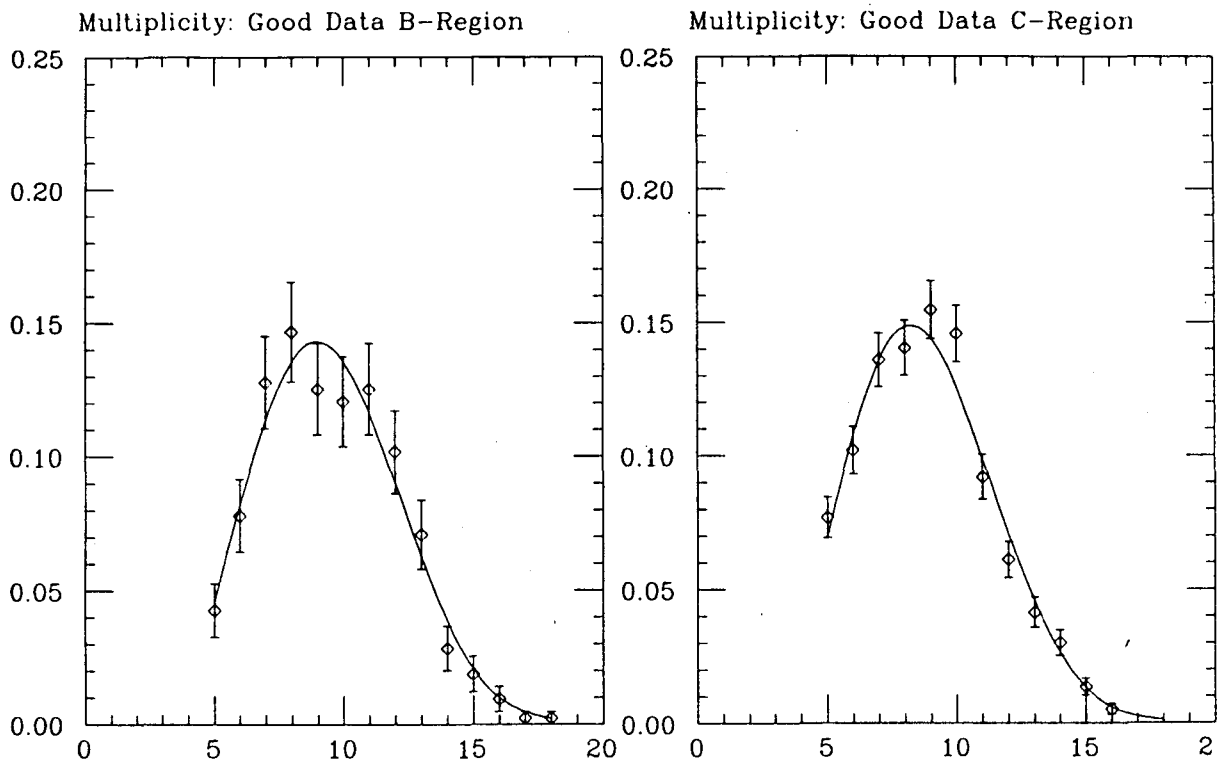

Figure 5.3: Same as Figure 5.2, using only the high efficiency data.

where all values are taken to be accurate to ±8%. Several corrections need to be applied to the solutions to these equations to obtain the final answer for the pure flavor mean multiplicities.

5.5 CORRECTIONS

Final corrections, determined from Monte Carlo analysis, are applied to the fit results to take account of effects that tend to bias our multiplicity measurement. Initial state radiation reduces the effective center of mass energy (E_{cm}) and hence the observed multiplicity. This effect is small, and is estimated by the following simple procedure:

1. Generate the Monte Carlo radiatively corrected E_{cm} distribution for selected hadronic events.
2. For the region from E_{cm} = 10.5 to 29 GeV (where statistics are significant), determine the drop in multiplicity by a convolution of the energy distribution

with a parameterization of multiplicity variation as a function of E_{cm}. For this purpose two such parameterizations are used,

a. A logarithmic dependence of the form : $n(E) = k_1 \log(E) + k_2$.

b. A QCD motivated dependence [45]: $n(E) = n_0 + a e^{b\sqrt{\ln(E^2/\Lambda^2)}}$. where the parameters have been chosen to fit the the data in Figure 5.4.

Taking the mean of the results due to the two different energy dependence functions and including a conservatively large error to allow for variation in the parameters, we obtain a correction of $+0.25 \pm 0.10$ particles. This is the only correction necessary for the average hadronic fit.

Secondly, the tagged region's lepton momentum lower limit of 2 GeV /c biases the data in favor of smaller multiplicities. As mentioned in the previous section, the same effect produces a small downward bias for the width parameters quoted above for the enriched samples and their backgrounds. By varying the lepton momentum cut for pure flavor Monte Carlo events, we determine these corrections, to be *added* to the final pure heavy flavor fit results, to be 0.3 ± 0.1 ($b\bar{b}$) and 0.9 ± 0.3 ($c\bar{c}$). The errors include statistical and systematic Monte Carlo uncertainties. The behavior of the Monte Carlo is consistent with the variation in fit results seen in the data if the lepton momentum cut is varied, and the appropriate flavor enrichment factors are used in equations 9. In any case, the corrected results are insensitive within errors to an increase in the lepton momentum cut of up to 500 MeV /c.

Finally, the requirement in the b-region that the lepton transverse momentum be at least 1 GeV /c tends to enrich the charm component of this region with high multiplicity three-jet events, a bias not present in the c-region. It has already been mentioned (see Table 5.1) that the gluon-jet content of the charm component in the b-region is about 65%, compared to a nominal 25%. We estimate from our Monte Carlo that the average produced multiplicity in three-jet events is higher than that for two jet events by ≈ 3.5 tracks regardless of the flavor (bottom or charm) of the quarks. This translates into a correction of $+1.5 \pm 0.7$ for the $c\bar{c}$ component in the b-region, accomplished by the modification of the appropriate term in equations 2 to $f_c^b(m_{c\bar{c}} + 1.5)$. A range of values for this correction factor from $0.5 - 2.5$ were used

to determine the corresponding corrections for the pure flavor results of: -0.4 ± 0.3 ($b\bar{b}$) and $+0.2 \pm 0.2$ ($c\bar{c}$).

5.6 Results and Discussion

The corrected solutions to equations 9 are given below, where the errors shown are purely statistical.

$$m_{b\bar{b}} = 14.85 \pm 0.5 \quad and \quad m_{c\bar{c}} = 12.95 \pm 0.5$$

Because the decay multiplicities depend on whether the decays are hadronic or semi-leptonic, care must be exersised in the interpretation of these numbers. These results represent the mean produced multiplicity of $b\bar{b}$ and $c\bar{c}$ events that have been tagged by our single lepton technique. The pecularities of the lepton tag need to be taken into account before our result can be cast into a fully measurement-independent form. Firstly, a fraction of the leptons in $b\bar{b}$ events are due to secondary semi-leptonic decays of charmed hadrons. Secondly, our single lepton event samples contain a small contamination of double lepton events in which one lepton was not identified. Both of these facts are relevant to the multiplicity measurement insofar as the multiplicities of semi-leptonic and hadronic heavy hadron decays are different. One needs to use the CLEO and SPEAR data for bottom and charm meson decay multiplicities to estimate these effects of the lepton tagging method .

We wish to determine the non-leading multiplicities which are of course independent of the heavy hadron decay mode, and we do so by subtracting out the leading multiplicities for our particular mix of hadronic and semi-leptonic decays. The known B and D-meson decay multiplicities for semileptonic and hadronic decay are given in Table 5.4 [25,14]. The B-meson multiplicities come directly from the CLEO measurements. The D-meson semi-leptonic decay multiplicities are calculated from the known semi-leptonic decay modes. The D-meson hadronic decay multiplicities are then deduced from the measured D meson mean decay multiplicities and their respective semi-leptonic branching ratios.

Heavy meson	Hadronic mult.	Semi-leptonic mult.
B-meson	6.0 ± 0.3	3.8 ± 0.4
$D^{\pm}$	2.31 ± 0.1	1.94 ± 0.1
D^0	2.47 ± 0.1	2.13 ± 0.1

Table 5.4 : Heavy hadron decay multiplicities.

The Monte Carlo is used to determine the relative populations of B, $D^{*\pm}$, D^{*o}, $D^{\pm}$ and D^o mesons in our tagged regions. The strange bottom mesons B_s^o are not distinguished from the B's, and the strange charm mesons $F^{\pm}$ are treated as if they were $D^{\pm}$'s. We have included the pion in the decay $D^{*\pm} \rightarrow D^o + \pi^{\pm}$ as part of the leading charm multiplicity. Neglecting the small contribution due to missed photon conversions, neither D^{*o} decay nor the radiative decays of B^* and F^* will add to the charged multiplicity. This procedure neglects possible small multiplicity differences due to heavy baryons or other charm and bottom states.

It is now relatively straightforward to estimate the effective leading multiplicity in our charm jets for both semi-leptonic and hadronic decays using the known branching ratios for D and D^* decays [13]; the results are 2.31 ± 0.1 and 2.64 ± 0.1 respectively. The CLEO collaboration has provided the corresponding results for B decay [25], but we must correct their semi-leptonic number for the component of secondary charm semi-leptonic decays in the b-region. The CLEO collaboration quotes a multiplicity of 3.5 ± 0.3 for the number of charged particles accompanying the D in hadronic B decay. We have already determined the relevant charm semi-leptonic decay multiplicity (2.31 ± 0.1). Knowing that the primary (direct B semi-leptonic decay) to secondary (semi-leptonic decay of the D from B decay) ratio in the b-region to be 7 : 1 from reference 26, we obtain 4.05 ± 0.4 for the effective semileptonic decay mean multiplicities in our bottom jets. The reader is reminded that the effective hadronic decay mean multiplicity in bottom jets is 6.0 ± 0.4.

The *total* leading multiplicity in the b and c-regions can now be calculated, but one must correct for the double lepton contamination. Defining $r \equiv \frac{\epsilon_2}{\epsilon_1}$ where ϵ_1 is the efficiency for observing a single lepton when one is produced, and ϵ_2 is

the efficiency for observing a single lepton when two are produced, the leading multiplicity for tagged events can be approximately written as,

$$n^{eff}_{leading} = f_1(n^{eff}_H + n^{eff}_{SL}) + f_2(2n^{eff}_{SL}) \tag{10}$$

with,

$$f_1 = \frac{2B(1-B)}{2B(1-B)+rB^2} \quad and \quad f_2 = \frac{rB^2}{2B(1-B)+rB^2}$$

and where B is the effective semi-leptonic branching ratio, and the n^{eff}'s are the semi-leptonic and hadronic effective leading jet multiplicities. For the b-region, B is taken to be 0.274, higher than the nominal value of 0.24 used in this thesis, in order to compensate for the contribution of secondary semi-leptonic decays. In the c-region, for a mix of charged and neutral charmed hadrons, the effective branching ratio is $B = 0.15$. The values of r are determined from the Monte Carlo to be $r_b = 1.2$ and $r_c = 1.6$. The resulting fully corrected total leading multiplicities for our tagged signal events are:

$$n^{b,eff}_{leading} = 9.69 \pm 0.5 \qquad n^{c,eff}_{leading} = 4.91 \pm 0.3$$

These numbers can be compared with the estimates of 10.05 ± 0.5 and 4.95 ± 0.2 obtained by ignoring the double lepton contamination; it can be seen that only the b-region correction is non-negligible, mainly due to the large difference in B-meson semi-leptonic and hadronic decay multiplicities.

The $non-leading$ multiplicities are given by:

$$n_{non-leading} = n_{fit} - n^{eff}_{leading} \tag{11}$$

The corrected event multiplicities for events with exactly one semi-leptonic and one hadronic decay are given by,

$$n_{SL/Had} = n_{non-leading} + n_{leading} \tag{12}$$

where the leading multiplicities used here are the fully detector independent values of 9.8 and 4.95 for bottom and charm respectively. One can also estimate the event

multiplicity for $b\bar{b}$ and $c\bar{c}$ with a nominal mixture of semi-leptonic and hadronic heavy hadron decays; a mixture given by the appropriate branching ratios. By combining the average hadronic mean multiplicity with these $b\bar{b}$ and $c\bar{c}$ results, one can estimate the light flavor (up, down and strange) mean event multiplicities. The final results, in the various forms mentioned above, are shown in Table 5.5.

	$b\bar{b}$	$c\bar{c}$	light quarks	all hadrons
1 S.L. and 1 Hadronic	$15.0 \pm 0.5 \pm 0.7$	$13.0 \pm 0.5 \pm 0.8$	—	—
Nominal mixture	$16.2 \pm 0.5 \pm 1.0$	$13.2 \pm 0.5 \pm 0.9$	$12.2 \pm 0.4 \pm 1.3$	$12.9 \pm 0.1 \pm 0.6$
Non-leading	$5.2 \pm 0.5 \pm 0.9$	$8.0 \pm 0.5 \pm 0.9$	—	—

Table 5.5 Mean Charged Multiplicities

The errors shown are the statistical and systematic errors respectively. The determination of systematic errors is described at the end of this chapter. Due to correlated systematic effects, the differences between the results for the separate flavors are more significant than the errors suggest; the bottom and charm results are different at greater than 99% confidence.

Some general observations can now be made:

1. The total multiplicity of bottom events is significantly higher than that for the lighter flavors, and the non-leading multiplicity of bottom events is significantly lower than that for charm events.
2. With regard to total multiplicity , charm events and average hadronic or light flavor (u,d,s) events are not measurably different.

These results are qualitatively in accord with our expectations. The known high multiplicity of b hadron decay is sufficiently greater than charm hadron decay multiplicity to overwhelm the compensating effect due to the lower non-leading multiplicity of $b\bar{b}$ events. Are the measured non-leading multiplicities quantitatively reasonable ? We can relate the non-leading multiplicities to the b and c quark fragmentation functions. The lower non-leading multiplicity for $b\bar{b}$ relative to $c\bar{c}$ provides independent evidence that b fragmentation is harder than c fragmentation. We can approximately translate these non-leading multiplicities to energies via ex-

isting multiplicity data for e^+e^- annihilation over a large range of center of mass energies shown in Figure 5.4 [45]. The procedure used here depends on the assumption that the relation between energy and multiplicity is unaffected by the flavor population of the events. The available multiplicity data are based on u,d,s,c,and b whereas our measured non-leading multiplicities arise from u,d,and s fragmentation. As shown in this analysis, this assumption is not exactly fulfilled, but the deviations are small enough to have no significant impact on the derived energy fractions.

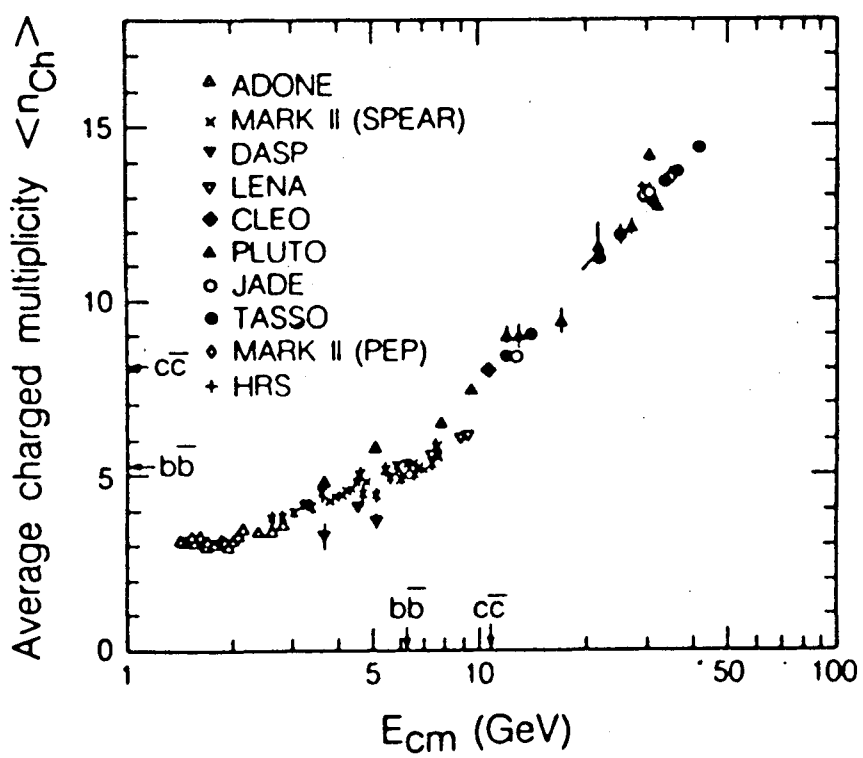

Figure 5.4: Multiplicity versus c.m. energy in e^+e^- annihilation. The non-leading multiplicities and their corresponding energies are shown for both bottom and charm events.

Using this information we find from the non-leading multiplicities that bottom

and charm hadrons fragment with mean energy fractions of

$$< z >_b = 0.79^{+0.10}_{-0.05} \quad and \quad < z >_c = 0.60^{+0.09}_{-0.11}$$

These results agree nicely with measurements based on leptonic inclusive spectra and D^* fragmentation, as shown in Figures 5.5 and 5.6 [20].

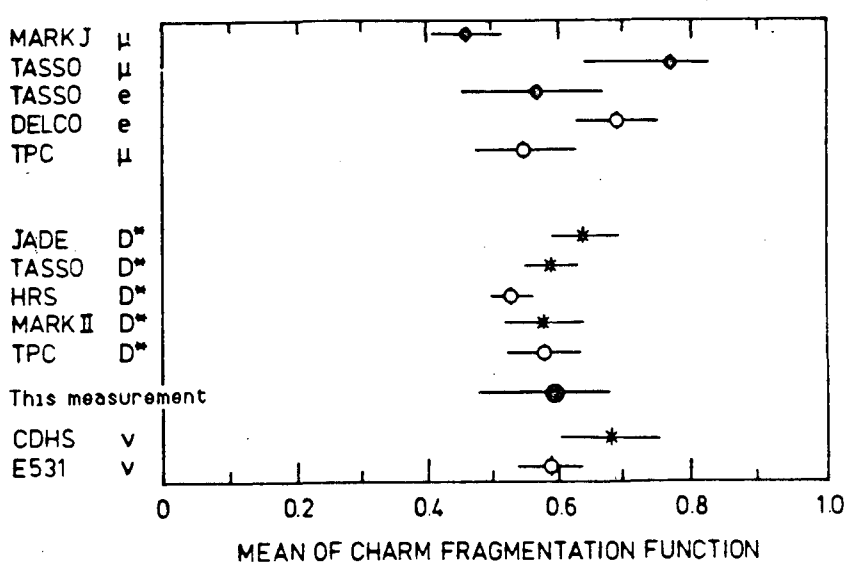

Figure 5.5: Charm fragmentation results from several experiments.

Our result for the *mean* charged multiplicity of hadronic events at 29 GeV agrees well with an analogous measurement due to the HRS collaboration at PEP [46]. We now turn to a discussion of the results for the *width* parameter of the hadronic multiplicity distribution. The TASSO collaboration at PETRA has measured the multiplicity of hadronic events at several c.m. energies including 22 and 34.5 GeV [45]. They perform a multi-parameter unfold and then compare the results with parent distribution functions analogous to the form of equation 2 with identical means and with the width parameter a fixed at 1 and 2. The TASSO

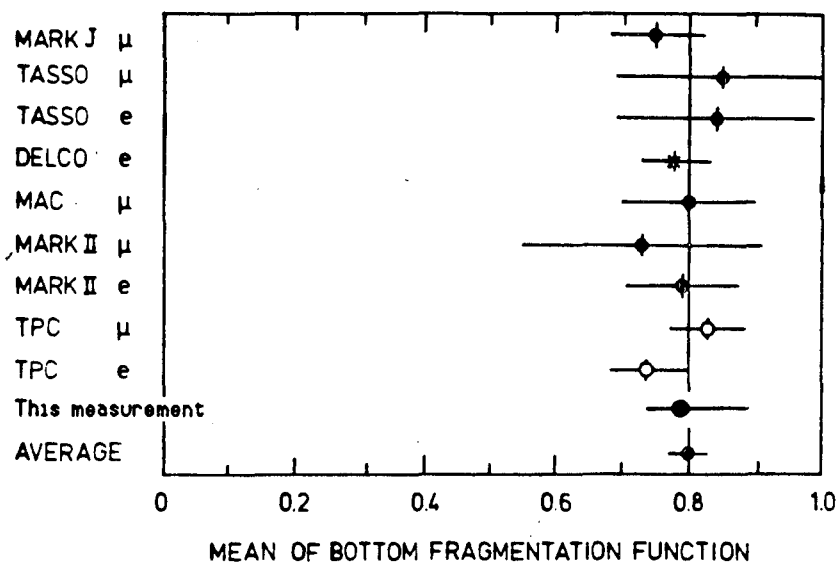

Figure 5.6: Bottom fragmentation results from several experiments.

analysis finds that the ordinary Poisson (a=1) slightly underestimates the unfolded distribution width, while the Poisson in the half population (a=2) is too wide. This observation is consistent with our fit result of $a = 1.4$. Another way to examine the dispersion of of multiplicity histograms is in the context of so-called Koba-Nielsen-Olesen (KNO) scaling [47]. The KNO hypothesis predicts energy scaling in a particular form of the multiplicity distribution. If $P(n)$ is taken to be probability density in multiplicity n, and $\overline{n}$ is the distribution mean, scaling should be evident in a plot of $P(n)\overline{n}$ versus $n/\overline{n}$. Figure 5.7, taken from reference 45, shows the KNO plot for e^+e^- annihilation at c.m. energies ranging from 5 to 34 GeV using the TASSO,JADE and LENA detectors. The curve is the Mark II result at 29 GeV where $P(n)$ is our best fit generalized Poisson function with width parameter $a = 1.4$. The agreement over this range of c.m. energies is quite good. We will not speculate as to whether this effect is evidence of a form of universal

behavior. The reader is instead referred to a selection of theoretical papers [48].

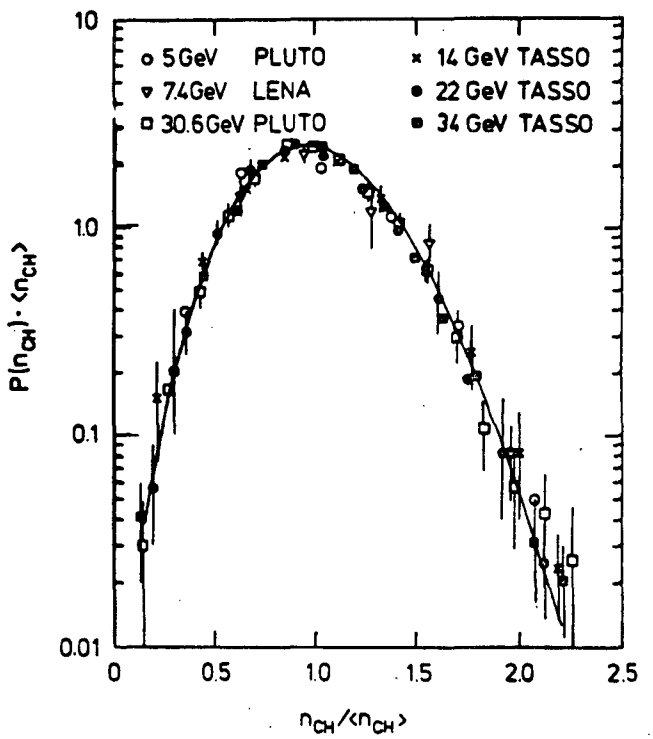

Figure 5.7: The KNO distribution for several experiments is shown along with our fit results for average hadronic events (solid curve).

5.7 Systematic Errors

The dominant sources of systematic error are the efficiency uncertainties in the event selection and track quality cuts (0.5), and the errors on the flavor composition percentages listed above (0.3: $b\bar{b}$, 0.5: $c\bar{c}$). These error were estimated by varing the relevant analysis cuts within experimentally reasonable limits, and by adjusting the composition factors within their quoted errors, and then reperforming the fits.

Other contributing factors include the details of the fitting procedure (0.2), the background simulation (0.1: $b\bar{b}$, 0.3: $c\bar{c}$) and the radiative and kinematic corrections discussed above (0.3). The fit was redone using single parameter fitting

functions and several different upper and lower truncations on the observed and produced multiplicity distributions in order to estimate the effect of our chosen fitting technique. The errors on the background means and the radiative and kinematic corrections were folded into the analysis, as were generous estimates of the systematic uncertainties in the background weighting procedure.

6. Conclusion

We have used the Mark II detector in the e^+e^- storage ring PEP at the Stanford Linear Accelerator Center (SLAC) to measure selected properties of hadronic events containing bottom or charm jets. Heavy flavor enrichment is accomplished by tagging events with high momentum electrons or muons, and bottom enrichment is then achieved by demanding that the lepton have high transverse momentum with respect to the event thrust axis. Differences between bottom and non-bottom jets are observed for momentum, transverse momentum, rapidity and jet mass distributions. Charm jets are found to be generally indistinguishable from average hadronic jets. The characteristic features of bottom jets stem mainly from two properties of bottom hadron weak decay : the high p_T and high multiplicity of the b-hadron decay products. Our observations on b-jets agree reasonably well with a Monte Carlo simulation based on (1) hard fragmentation of b quarks and (2) b decay properties as measured from experiments at the CLEO detector. A detailed study of the charged multiplicity of b- and c-enriched events finds the mean multiplicity of bottom and charm events to be $16.2 \pm 0.5 \pm 1.0$ and $13.2 \pm 0.5 \pm 0.9$ respectively, where the first error is statistical and the second systematic. The corresponding non-leading multiplicities of charged particles accompanying the pair of heavy hadrons are $5.2 \pm 0.5 \pm 0.9$ for bottom, and $8.0 \pm 0.5 \pm 0.9$ for charm. We find from these non-leading multiplicities that bottom and charm hadrons fragment with mean energy fractions of

$$< z >_b = 0.79^{+0.10}_{-0.05} \quad and \quad < z >_c = 0.60^{+0.09}_{-0.11}$$

These results confirm the expected hard fragmentation of heavy quarks and agree with previous measurements based on leptonic inclusive spectra and D^* fragmentation.

REFERENCES

1. See for example D. J. Gross and F. Wilczek, Phys. Rev. D. 8, 3633 (1973).
2. D. J. Gross and F. Wilczek , Phys. Rev. Lett. 30, 1343 (1973).
3. H. D. Politzer , Phys. Rev. Lett. 30, 1346 (1973).
4. R. Field and R. Feynman, Nucl. Phys. B136, 1, (1978).
5. B. Andersson et al., Phys. Rep. 97, 31 (1983).
6. G. Marchesini and B. Weber, Nucl. Phys. B238, 1, (1984), B. Weber, Nucl. Phys. B238, 492, (1984).
7. Quark pair production from the vacuum can be described as a quantum tunneling process, with a resulting exponential suppression of massive pairs. See for example J. Schwinger, Phys. Rev. 82, 664 (1951), or H. Bohr and H. B. Nielson, NBI-HE-78-3 (1978).
8. S. Weinberg , Phys. Rev. Lett. 19, 1264 (1967).
9. A. Salam, Elementary Particle Theory, ed. N. Svartholm, p.367 (1968).
10. S. L. Glashow, J. Iliopoulos and L. Maiani Phys. Rev. D. 2, 1285 (1970).
11. M. Kobayashi and T. Maskawa, Prog. Theor. Phys. 49, 652, (1973).
12. Stanley Wojcicki in Proceedings of the Twelfth SLAC Summer Institute on Particle Physics, SLAC-Report 281, edited by Patricia M. McDonough, Stanford CA, 175 (1984).
13. C. G. Wohl et al., Particle Data Group, Rev. Mod. Phys. 56, S1 (1984).
14. R. H. Schindler et al., Phys. Rev. D 24, 78 (1981).
15. J. Jaros in Proceedings of the International Conference on Instrumentation for Colliding Beam Physics, SLAC-Report 250, edited by W. Ash, Stanford CA, 29 (1982).
16. T. Himel, thesis, Stanford University, SLAC-223 (1979)
17. M. Suzuki, Phys. Lett. 71*B*, 139 (1977).
18. B. J. Bjorken, Phys. Rev. D. 17, 171 (1978).
19. C. Peterson et al., Phys. Rev. D. 27, 105 (1983).
20. see J. M. Izen, DESY 84-104 (1984) for a review of heavy quark fragmentation results.

21. H. Schellman, thesis, University of California, Berkeley, LBL-18699 (1984).

22. W. Bacino et al., Phys. Rev. Lett. 43, 1073 (1979).

23. K. Chadwick et al., Phys. Rev. D. 27, 475 (1983).

24. A. Ali et al., Z. Phys. C2, 33, (1979).

25. R. Giles et al., Phys. Rev. D. 30, 2279 (1984).

26. M. E. Nelson, thesis, University of California, Berkeley, LBL-16724 (1983).

27. M. E. Nelson et al., Phys. Rev. Lett. 50, 1542 (1983).

28. A. Ali, Z. Phys. C1, 25, (1979).

29. T. P. Schaad et al., SLAC-PUB-3696, May (1985) submitted to Phys. Lett. B.

30. H. M. Schellman, Trilling/Goldhaber Technical Note, No.247, (1983).

31. M. Althoff et al. ,Phys. Lett. 135B, 243 (1981),also give a multiplicity measurement for charm jets opposite to a D^* tag at 34.5 GeV

32. M. Sakuda et al., CALT-68-1164 (1984), submitted to Phys. Lett., also give a multiplicity measurement for bottom jets opposite to a lepton tag at 29 GeV.

33. T. P. Schaad, SLAC/Mark II Memo., March 20, (1985).

34. M. Althoff et al. ,Phys. Lett. 149B, 524 (1984). This analysis uses a variant of the event sphericity to select b-events.

35. P. Steffen, 22nd International Conference on High Energy Physics, Leipzig (1984). A combination of lepton tagging and a selection based on event planarity is used here for b-enrichment.

36. E. Fernandez et al., Phys. Rev. Lett. 50, 2054 (1983).

37. B. Adeva et al., Phys. Rev. Lett. 51, 443 (1983).

38. M. Althoff et al., Z. Phys. C22, 219, (1984).

39. D. E. Koop et al., Phys. Rev. Lett. 52, 970 (1984).

40. J. M. Yelton et al., Phys. Rev. Lett. 49, 430 (1982).

41. P. Avery et al., Phys. Rev. Lett. 51, 1139 (1983).

42. M. Derrick et al., Phys. Lett. 146*B*, 261 (1984).

43. M. W. Coles, thesis, University of California, Berkeley, LBL-11513 (1980).

44. F. James and M. Roos, MINUIT, CERN program library no.D506

45. M. Althoff et al., Z. Phys. C22, 307, (1984).

46. D. Bender et al., Phys. Rev. D. 31, 1 (1985).

47. Z. Koba, H. B. Nielsen and P. Olesen, Nucl. Phys. B40, 317, (1972).

48. For example, P. Carruthers and C. C. Shih, Phys. Lett. 127*B*, 242 (1983) or G. Pancheri, CERN EP/84-96, (1984).

This report was done with support from the Department of Energy. Any conclusions or opinions expressed in this report represent solely those of the author(s) and not necessarily those of The Regents of the University of California, the Lawrence Berkeley Laboratory or the Department of Energy.

Reference to a company or product name does not imply approval or recommendation of the product by the University of California or the U.S. Department of Energy to the exclusion of others that may be suitable.

LAWRENCE BERKELEY LABORATORY
TECHNICAL INFORMATION DEPARTMENT
UNIVERSITY OF CALIFORNIA
BERKELEY, CALIFORNIA 94720